ISLAMIC UNIVERSITY OF TECHNOLOGY

Parameter Extraction of Optical Materials and Investigation of Surface Plasmon Polariton (SPP) Propagation in Different Optical Nanostructures

By:

Md. Ghulam Saber (092416)

Asif Al Noor (092417)

Md. Thesun Al-Amin (092434)

A thesis submitted in partial fulfillment of the requirements
for the degree of Bachelor of Science in Electrical and Electronic Engineering

Academic Year: 2012-2013

Department of Electrical and Electronic Engineering

Islamic University of Technology.

A Subsidiary Organ of the Organisation of Islamic Cooperation (OIC).

Dhaka, Bangladesh.

October 2013

Parameter Extraction of Optical Materials and Investigation of Surface Plasmon Polariton (SPP) Propagation in Different Optical Nanostructures

By:
Md. Ghulam Saber (092416)
Asif Al Noor (092417)
Md. Thesun Al-Amin (092434)

Supervised By:
Rakibul Hasan Sagor
Assistant Professor,
Department of Electrical and Electronic Engineering,
Islamic University of Technology.

A thesis submitted in partial fulfillment of the requirements
for the degree of Bachelor of Science in Electrical and Electronic Engineering

Academic Year: 2012-2013

Department of Electrical and Electronic Engineering
Islamic University of Technology.
A Subsidiary Organ of the Organisation of Islamic Cooperation (OIC).
Dhaka, Bangladesh.

Declaration of Authorship

We, Md. Ghulam Saber (092416), Asif Al Noor (092417) and Md. Thesun Al-Amin (092434), declare that this thesis titled, 'Parameter Extraction of Optical Materials and Investigation of Surface Plasmon Polariton (SPP) Propagation in Different Optical Nanostructures' and the works presented in it are our own. We confirm that:

- This work has been done for the partial fulfillment of the Bachelor of Science in Electrical and Electronic Engineering degree at this university.
- Any part of this thesis has not been submitted anywhere else for obtaining any degree.
- Where we have consulted the published work of others, we have always clearly attributed the sources.

Submitted By:

_____

Md. Ghulam Saber (092416)

_____

Asif Al Noor (092417)

_____

Md. Thesun Al-Amin (092434)

Parameter Extraction of Optical Materials and Investigation of Surface Plasmon Polariton (SPP) Propagation in Different Optical Nanostructures

Approved By:

Rakibul Hasan Sagor
Thesis Supervisor,
Assistant Professor,
Department of Electrical and Electronic Engineering,
Islamic University of Technology.

Prof. Dr. Md. Shahid Ullah
Head of the Department,
Department of Electrical and Electronic Engineering,
Islamic University of Technology.

ISLAMIC UNIVERSITY OF TECHNOLOGY

Abstract

Department of Electrical and Electronic Engineering

Bachelor of Science in Electrical and Electronic Engineering

Parameter Extraction of Optical Materials and Investigation of Surface Plasmon Polariton (SPP) Propagation in Different Optical Nanostructures

by Md. Ghulam Saber (092416), Asif Al Noor (092417) and Md. Thesun Al-Amin (092434)

The ability of Surface-Plasmon-Polaritons (SPPs) to overcome the diffraction limit has made it a field of great research interest. It is being predicted that next generation microchips will be produced using plasmonics-electronics hybrid technology. This will solve the RC-delay issue of current electronic microchips and scaling issue of conventional integrated photonic devices. However, there are some shortcomings of SPP which are higher losses in the metallic layer and less propagation distance. Using current technology, propagation distance of SPP cannot exceed the benchmark of micrometers. The objective of this thesis is to extract the modeling parameters for several materials and analyze their performance using the FDTD method. The modeling parameters have been extracted using an optimization algorithm. The parameters were then used to define different materials in the simulation model. SPP propagation characteristics through different optical nanostructures having different geometries have been investigated to analyze the performance of the materials. Finally, simple nanoplasmonic coupling structures using gallium lanthanum sulfide and cuprous oxide have been proposed and investigated that provide appreciable performance.

Acknowledgements

First and foremost, we offer gratitude to the Almighty Allah (SWT) for giving us the capability to do this work with good health.

We are grateful to our research supervisor, Rakibul Hasan Sagor, for the support and guidance throughout our research at Islamic University of Technology (IUT) since July, 2012. He created a research environment for which we were able to explore many ideas without constraint. We have gained a wealth of knowledge and experience in science and engineering through his direction that is beyond value to our future endeavour. For these things, we give many thanks to him.

We would like to thank all the faculty members of the department of EEE, IUT for their inspiration and help.

And last but not the least we are thankful to our family, friends and well-wishers for their support and inspiration. Without them it would never have been possible for us to make it this far.

Contents

List of Figures

List of Tables

Abbreviations

ABC	**A**bsorbing **B**oundary **C**ondition
ADE	**A**uxiliary **D**ifferential **E**quation
AlGaAs	**Al**uminum **Ga**llium **A**rsenide
DMD	**D**ielectric-**M**etal-**D**ielectric
FDTD	**F**inite **D**ifference **T**ime **D**omain
GLS	**G**allium **L**anthanum **S**ulfide
IR	**I**nfra-**R**ed
LD	**L**orentz-**D**rude
MDM	**M**etal-**D**ielectric-**M**etal
PLRC	**P**iecewise **L**inear **R**ecursive **C**onvolution
PML	**P**erfectly **M**atched **L**ayer
SiGe	**Si**licon **Ge**rmanium alloy
SPP	**S**urface **P**lasmon **P**olariton
TE	**T**ransverse **E**lectric
TM	**T**ransverse **M**agnetic
VSWR	**V**oltage **S**tanding **W**ave **R**atio

Dedicated to our parents. . . .

Chapter 1

Introduction and Background

Since the inception of modern science, we have tried to manipulate light in order to enhance our optical perception. Recent advances in the fabrication technology have made it possible to exploit the light-matter interaction at the nanoscale which has enabled us to visualize varieties of natural phenomenon. Ability to confine light into nanoscale has opened the door for multitude of applications which have never been thought of before. At present, the communication system is fully dependent on the optical fibers which offer high bandwidth and low loss than electronic interconnections. The same advantage can be availed if the optical technology is used in computer chips. Also, the optical chips will not require any insulation since photons do not interact with each other, making the system lighter [3] [4]. However, the diffraction limit of light restricts the application of conventional optics in making nanometer scale integrated circuits. According to the diffraction limit rule, light cannot propagate through aperture that is smaller than half of its wavelength.

The diffraction limit can be overcome by making the use of light-matter interaction at metal surface [5] [6]. A new type of electromagnetic wave called Surface-Plasmon-Polariton (SPP) is generated at the metal surface due to the coupling of photon and electron when metal is exposed to light in a certain way. The ability of SPP to overcome the diffraction limit has opened the horizon of multitude of new applications.

The computation power of computer chips will be increased if plasmonic based integrated circuits can be designed. Researchers have already demonstrated functional plasmonic nanocircuits experimentally [7]. The day is not far when plasmonic chips will also be available.

Researchers have achieved enormous performance improvement in solar cell technology using plasmonics. The absorption efficiency has increased significantly by implementing plasmon enhanced solar cells [8] [9] [10].

Plasmonics is also being applied in the field of imaging [11] [12] [13] [14], biosensing [15], bragg reflector [16] and metamaterials [17].

1.1 Overview of Surface-Plasmon-Polariton

Surface plasmon polaritons are electromagnetic excitations propagating at the interface between a dielectric and a conductor, evanescently confined in the perpendicular direction [18]. These electromagnetic surface waves arise via the coupling of the electromagnetic fields to oscillations of the conductor's electron plasma.

The eigenmodes of an interface between a dielectric and a metal are surface plasmon polaritons (SPPs) [19]. We refer to them as eigenmodes in the sense that they are solutions of Maxwell's equations that can be formulated in the absence of an incident field [20]. On a flat interface between dielectric and metal half-spaces with dielectric constants ε_d and ε_m, respectively, SPPs are transverse magnetic (TM) plane waves propagating along the interface. Assuming the interface is normal to z and the SPPs propagate along the x direction, the SPP wavevector k_x is related to the optical frequency through the dispersion relation [21]

$$k_x = k_o\sqrt{\varepsilon_d\varepsilon_m/(\varepsilon_d + \varepsilon_m)} \tag{1.1}$$

where, $k_o = \omega/c$ is the free-space wavevector. We take ω to be real and allow k_x to be complex, since our main interest is in stationary monochromatic SPP fields in a finite area [22]. The details of SPP has been discussed in **Chapter 2**.

1.2 Literature Review

Surface-Plasmon-Polaritons have been a field of great research interest for the past few years. Several research works have been done on this topic. Material modeling is another vast field of research where many researchers are working on. The main focus of the literature review will be on the published works related to material modeling parameter extraction and SPP propagation analysis through different structures with different geometries.

The parameters of several metals have been reported to our knowledge. Jin et al. [23] determined the modified Debye model parameters for gold which are applicable in the wavelength range of 550-950 nm. Krug et al. [24] reported the gold parameters that are applicable in the wavelength range of 700-1000 nm. W.H.P. Pernice et al. [25] extracted the parameters for Nickel using Lorentz-Drude model. A.D. Rakic et al. [26] reported the parameters for Nickel, Palladium, Titanium and 8 other metals using Lorentz-Drude and Brendel-Bormann Model. M.A. Ordal et al. [27] extracted the parameters for fourteen metals in the infrared and far-infrared range.

Bends, splitters and recombinations are inevitable parts of the optoelectronic devices. Several works on the analysis of SPP propagation in these shapes have been reported to our knowledge. G. Veronis et al. [28] showed that bends and splitters can be designed over a wide frequency range without much loss by keeping centre layer thickness small compared to wavelength. H. Gao et al. [29] investigated the propagation and combination of SPP in Y-shaped channels. B. Wang et al. [30] analyzed two structures which consist of splitting and recombination.

The propagation loss of SPP is very high in metal-dielectric-metal configuration of plasmonic waveguide which limits the length of propagation. Even the fabrication related disorders have far less impact on the propagation loss than the losses that occur in metallic layers of the MDM waveguide. This problem can be addressed by using both dielectric and plasmonic waveguide on the same chip. The dielectric waveguide will carry the fundamental optical mode while the plasmonic waveguide will address the sub-wavelength scale issue. This calls for the need of efficient coupling of optical modes from the dielectric waveguide to the plasmonic waveguide. Therefore, designing efficient nanoplasmonic couplers with different materials and structures can be a pioneering step in miniaturization of the integrated photonic devices. In the past years, several plasmonic couplers have been proposed by different researchers. G. Veronis et. al. [1] proposed a coupler with multi-section tapers. P. Ginzburg et al. [31] reported a $\lambda/4$ coupler to couple optical modes from a 0.5m to 50nm wide plasmonic waveguide. D. Pile et al. [32] presented an adiabatic and a non-adiabatic tapered plasmonic coupler. R. Washleh et al. [2] reported an analysis on nanoplasmonic air-slot coupler and its fabrication steps.

1.3 Thesis Objective

The main objective of the thesis is to extract the modeling parameters for different linear dispersive material and use those material modeling parameters to study the SPP propagation in different optical nanostructures. However, more specifically, the objectives are

- To extract the linear dispersive modeling parameters for different metals and dielectric materials. This includes literature review, collection of data, development of optimization algorithm etc.
- To develop a simulation model based on the FDTD method that is capable of simulating the properties of linear dispersive materials.
- To construct different optical nanostructure using the extracted material modeling parameters and simulate the SPP propagation in those structures.
- To summarize important conclusions from the obtained results and discuss the potential applications.

1.4 Thesis Organisation

The thesis has been arranged in the following way-

- In **Chapter 2**, the basic theory of SPP propagation has been described. This chapter introduces the fundamental knowledge and necessary mathematical formulations of SPP propagation at the single and double interface.
- In **Chapter 3**, the widely used models for modeling metals have been described in detail with necessary derivations. Since SPPs are created due to the coupling of photon energy to the free electrons of metal, modeling metals is one of the key steps for the simulation of SPP propagation.
- Since we have developed our simulation model based on FDTD method, **Chapter 4** introduces the fundamentals of the FDTD algorithm for 1D and 2D simulations. The original formulations of Yee do not include the frequency dependent dispersion properties of materials. We have used the ADE based general algorithm for our simulation model which is discussed in **Chapter 4**. This chapter also discusses about the absorbing boundary condition.

- **Chapter 5** discusses the optimization method that has been used to extract the modeling parameters of the optical materials. The obtained modeling parameters and their validations are also provided in this chapter.
- We have used the extracted modeling parameters to simulate SPP propagation through different optical nanostructures constructed with those materials. In **Chapter 6**, the simulation results for SPP propagation through different structures are provided.
- In **Chapter 7**, we have provided the concluding remarks about our work and our future plans with the thesis.

Chapter 2

SPP Propagation Theory

2.1 Introduction

Surface plasmon polariton (SPP) is an electromagnetic excitation that propagates in a wave like fashion along the planar interface between a metal and a dielectric medium, often vacuum, and whose amplitude decays exponentially with increasing distance into each medium from the interface. Electromagnetic wave propagation is obtained from the solution of Maxwell's equations in each medium, and the associated boundary conditions. Maxwell's equations of macroscopic electromagnetism can be written as follows:

From Gauss's Law for the electric field

$$\nabla.D = \rho_{ext} \tag{2.1}$$

From Gauss's Law for the magnetic field,

$$\nabla.B = 0 \tag{2.2}$$

From Faraday's Law

$$\nabla \times E = -\frac{\partial B}{\partial t} \tag{2.3}$$

From Ampere's Law

$$\nabla \times H = J_{ext} + \frac{\partial D}{\partial t} \tag{2.4}$$

Here,

E is the electric field vector in volt per meter

D is the electric flux density vector in coulombs per square meter

H is the magnetic field vector in amperes per meter

B is the magnetic flux density vector in webbers per square meter

ρ_{ext} is the charge density

J_{ext} is the current density

The four macroscopic fields can be also linked further via the polarization P and magnetization M by

$$D = \varepsilon_0 E + P \tag{2.5}$$

$$H = \frac{1}{\mu_0} B - M \tag{2.6}$$

Now this equations can be simplified for linear, isotropic, nonmagnetic media as

$$D = \varepsilon_0 \varepsilon_r E \tag{2.7}$$

$$B = \mu_0 \mu_r H \tag{2.8}$$

where,

ε_0 is electric permittivity of vacuum in Farad per meter

μ_0 is the magnetic permeability of vacuum in Henry per meter

ε_r is the relative permittivity

μ_r is the relative permeability

2.2 The EM or Electromagnetic Wave Equation

The EM wave equation which describes the field amplitude in time and space can be derived from Maxwell's equations. The wave equation can be derived by taking curl of Faraday's law

$$\nabla \times \nabla \times E = -\frac{\partial B}{\partial t} \tag{2.9}$$

or,

$$\nabla \times \nabla \times E = \nabla \times \left(-\mu \frac{\partial H}{\partial t}\right) \tag{2.10}$$

with the identities $\nabla \times \nabla \times E = \nabla (\nabla . E) - \nabla^2 E$ and $\nabla \times H = \varepsilon \frac{\partial E}{\partial t}$ we can simplify the above equation as

$$\nabla (\nabla . E) - \nabla^2 E = -\mu \varepsilon \frac{\partial^2 E}{\partial t^2} \tag{2.11}$$

From Gauss's law we can conclude that the divergence of E in a constant permittivity over space is zero. i,e $\nabla . E = 0$

Therefore, the final wave equation for electric field will be

$$\nabla^2 E - \mu \varepsilon \frac{\partial^2 E}{\partial t^2} = 0 \tag{2.12}$$

Similarly the wave equation for magnetic field can be derived as

$$\nabla^2 H - \mu \varepsilon \frac{\partial^2 H}{\partial t^2} = 0 \tag{2.13}$$

So, the general form of wave equation can be written as

$$\nabla^2 U - \frac{1}{v_p^2}\left(\frac{\partial^2 H}{\partial t^2}\right) = 0 \tag{2.14}$$

If the variation of the dielectric profile ε is negligible over distance, then we can write

$$\nabla^2 E - \frac{\varepsilon}{c^2}\frac{\partial^2 E}{\partial t^2} = 0 \tag{2.15}$$

where $c = \frac{1}{\sqrt{\mu_0 \varepsilon_0}}$, velocity of light.

The solution of wave equation is a harmonic function in time and space. Now if we assume this as a harmonic time dependence of the electric field,

$$E(r,t) = E(r)\, e^{-jwt} \tag{2.16}$$

Therefore we get the Helmholtz equation

$$\nabla^2 E + k_0^2 \varepsilon E = 0 \tag{2.17}$$

where the vector of propagation $k_0 = \frac{\omega}{c}$, in free space

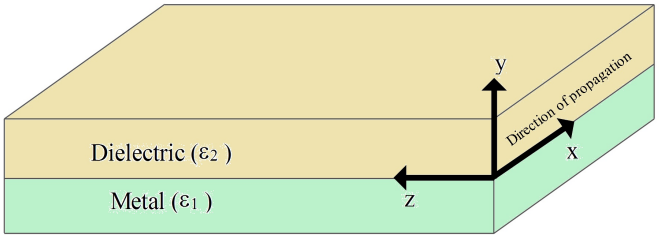

FIGURE 2.1: Typical planar waveguide geometry. The waves propagate along the x-direction in a cartesian coordinate system.

For simplicity let us assume the propagation of wave is along the x-direction of the Cartesian co-ordinate system and no spatial variation in y-direction. So we can write

$$E(x, y, z) = E(z)\, e^{j\beta x} \tag{2.18}$$

where $\beta = k_x$ which is call the propagation constant.

Now inserting the value of E the wave equation will be

$$\frac{\partial^2 E(z)}{\partial z^2} + \left(k_0^2 \varepsilon - \beta^2\right) E = 0 \tag{2.19}$$

Similarly we can derive the equation for the magnetic field H. The field E and H can be decomposed in cartesian co-ordinate system as

$$E = E_x.\overrightarrow{a_x} + E_y.\overrightarrow{a_y} + E_z.\overrightarrow{a_z} \tag{2.20}$$

$$H = H_x.\overrightarrow{a_x} + H_y.\overrightarrow{a_y} + H_z.\overrightarrow{a_z} \tag{2.21}$$

For Harmonic time dependence $\frac{\partial}{\partial t} = -j\omega$ and by solving the Ampere's law and Faraday's law, we get

$$\frac{\partial E_z}{\partial y} - \frac{\partial E_y}{\partial z} = j\omega\mu_0 H_x \tag{2.22}$$

$$\frac{\partial E_x}{\partial z} - \frac{\partial E_z}{\partial x} = j\omega\mu_0 H_y \tag{2.23}$$

$$\frac{\partial E_y}{\partial x} - \frac{\partial E_x}{\partial y} = j\omega\mu_0 H_z \tag{2.24}$$

$$\frac{\partial H_z}{\partial y} - \frac{\partial H_y}{\partial z} = -j\omega\varepsilon_0\varepsilon E_x \tag{2.25}$$

$$\frac{\partial H_x}{\partial z} - \frac{\partial H_z}{\partial x} = -j\omega\varepsilon_0\varepsilon E_y \tag{2.26}$$

$$\frac{\partial H_y}{\partial x} - \frac{\partial H_x}{\partial y} = -j\omega\varepsilon_0\varepsilon E_z \tag{2.27}$$

As the propagation is in x-direction in the form of $e^{j\beta x}$ which follows that $\frac{\partial}{\partial x} = -j\beta$. The homogeneity in y- direction makes $\frac{\partial}{\partial y} = 0$. So the equation will be simplified as

$$-\frac{\partial E_y}{\partial z} = j\omega\mu_0 H_x \tag{2.28}$$

$$\frac{\partial E_x}{\partial z} - j\beta E_z = j\omega\mu_0 H_y \tag{2.29}$$

$$j\beta E_y = j\omega\mu_0 H_z \tag{2.30}$$

$$\frac{\partial H_y}{\partial z} = j\omega\varepsilon_0\varepsilon E_x \tag{2.31}$$

$$\frac{\partial H_x}{\partial z} - j\beta H_z = -j\omega\varepsilon_0\varepsilon E_y \tag{2.32}$$

$$j\beta H_y = -j\omega\varepsilon_0\varepsilon E_z \tag{2.33}$$

The solution of the above equation can be characterized by two sets of solution with the polarized characteristics which are, Transverse Magnetic (TM) modes and Transverse Electric (TE) modes. The equations belong to TM modes are

$$E_x = -j\frac{1}{\omega\varepsilon_0\varepsilon}\frac{\partial H_y}{\partial z} \tag{2.34}$$

$$E_z = -\frac{\beta}{\omega\varepsilon_0\varepsilon}H_y \tag{2.35}$$

Therefore, the wave equation for TM Polarized wave will be

$$\frac{\partial^2 H_y}{\partial z^2} + \left(k_0^2\varepsilon - \beta^2\right)H_y = 0 \tag{2.36}$$

Similarly the TE polarized equations will be

$$H_x = j\frac{1}{\omega\mu_0}\frac{\partial E_y}{\partial z} \tag{2.37}$$

$$H_z = \frac{\beta}{\omega\mu_0}E_y \tag{2.38}$$

And the corresponding TE wave equation will be

$$\frac{\partial^2 E_y}{\partial z^2} + \left(k_0^2\varepsilon - \beta^2\right)E_y = 0 \tag{2.39}$$

2.3 SPP at Single Interface

The simplest configuration of SPP propagation is at single interface, that is in between dielectric, having the positive dielectric constant ε_2 and metal, having the negative dielectric constant ε_1. For metal the bulk plasmon frquency will be ω_p and the amplitude decays perpendicular to the $z-$ direction.

For the TM solutions in both spaces: metal and dielectric will be for $z > 0$

$$H_z(z) = A_2 e^{j\beta x}e^{-k_2 z} \tag{2.40}$$

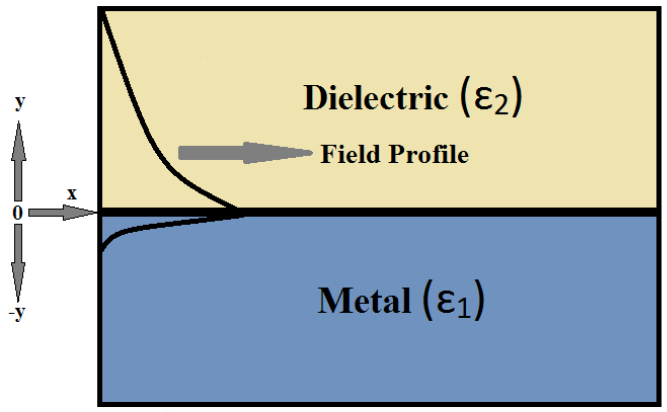

FIGURE 2.2: SPP at the Single interface.

$$E_x(z) = jA_2 \frac{1}{\omega\varepsilon_0\varepsilon_2} k_2 e^{j\beta x} e^{-k_2 z} \tag{2.41}$$

$$E_z(z) = -A_1 \frac{\beta}{\omega\varepsilon_0\varepsilon_2} e^{j\beta x} e^{-k_2 z} \tag{2.42}$$

And for $z < 0$

$$H_y(z) = A_1 e^{j\beta x} e^{k_1 z} \tag{2.43}$$

$$E_x(z) = -jA_1 \frac{1}{\omega\varepsilon_0\varepsilon_1} k_1 e^{j\beta x} e^{k_1 z} \tag{2.44}$$

$$E_x(z) = -A_1 \frac{\beta}{\omega\varepsilon_0\varepsilon_1} e^{j\beta x} e^{k_1 z} \tag{2.45}$$

The continuity of H_y and $\varepsilon_i E_z$ at the metal dielectric interface gives $A_1 = A_2$ and

$$\frac{k_2}{k_1} = -\frac{\varepsilon_2}{\varepsilon_1} \tag{2.46}$$

The surface wave exists at the metal dielectric interface with opposite sign of their real dielectric permittivities. So, we can write

$$k_1^2 \varepsilon = \beta^2 - k_0^2 \varepsilon_1 \tag{2.47}$$

$$k_2^2\varepsilon = \beta^2 - k_0^2\varepsilon_2 \tag{2.48}$$

The dispersion relation of SPPs propagation can be found as

$$\beta = k_0\sqrt{\frac{\varepsilon_1\varepsilon_2}{\varepsilon_1+\varepsilon_2}} \tag{2.49}$$

The TE surface modes can be expressed as

$$E_y(z) = A_2 e^{j\beta x}e^{-k_2 z} \tag{2.50}$$

$$H_x(z) = -jA_2\frac{1}{\omega\mu_0}k_2 e^{j\beta x}e^{-k_2 z} \tag{2.51}$$

$$H_z(z) = -A_2\frac{\beta}{\omega\mu_0}e^{j\beta x}e^{-k_2 z} \tag{2.52}$$

for $z > 0$, and

$$E_y(z) = A_1 e^{j\beta x}e^{k_1 z} \tag{2.53}$$

$$H_x(z) = jA_1\frac{1}{\omega\varepsilon_0\varepsilon_1}k_1 e^{j\beta x}e^{k_1 z} \tag{2.54}$$

$$H_z(z) = A_1\frac{\beta}{\omega\varepsilon_0\varepsilon_1}e^{j\beta x}e^{k_1 z} \tag{2.55}$$

for $z < 0$. The continuity of E_y and H_x requires

$$A_1(k_1 + k_2) = 0 \tag{2.56}$$

The surface requires that the real part of k_1 and k_2 should be greater than zero for confinement. This will be satisfied if $A_1 = A_2 = 0$. Therefore no surface modes for the TE polarization. SPP only exist for TM mode polarization.

2.4 SPP at Double Interface

Two mostly used double interface configurations of SPP waveguides are: Metal-Dielectric-Metal(MDM) and Dielectric-Metal-Dielectric (DMD). In these cases SPPs are formed on both interfaces. When the distance is shorter than decay distance, it forms coupled mode of SPP. This coupled mode of propagation can also be sub-divided into even and odd modes, as shown in the figure

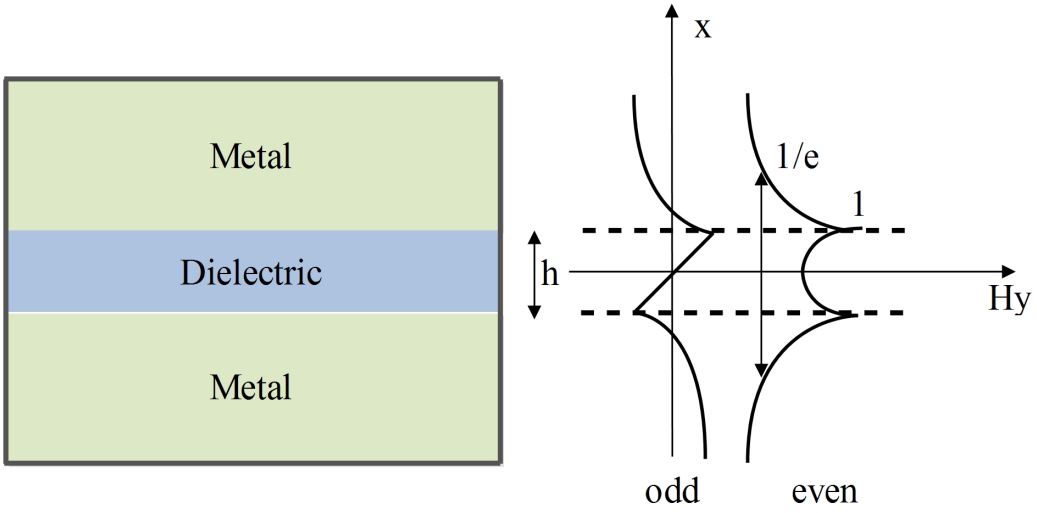

FIGURE 2.3: SPP at the double interface.

Chapter 3

Material Modeling Within Optical Range

3.1 Introduction

At low frequencies or for long wavelengths metals act as perfect conductors. Since it has zero field, they do not show any dispersive behavior. But at higher frequencies such as optical range metals behave as dispersive materials which means that there exists field inside metal. And for the frequencies higher than optical range metals act as dielectrics. Properties of SPPs depend highly on the material response to light. In this chapter we will be studying about the material supporting SPP, descriptions and derivations of different models for describing the behavior of metal in the presence of light.

Now in prsence of an external oscillating electromagnetic field, three vectors can determine the behavior of any material. Such as: D (electrical flux density), E (electric field intensity) and P (polarization density). In frequency domain the corresponding eqation will be

$$D(\omega) = \varepsilon(\omega) E(\omega) \tag{3.1}$$

$$P(\omega) = \varepsilon_0 \chi(\omega) E(\omega) \tag{3.2}$$

$$D(\omega) = \varepsilon_0 E(\omega) + P(\omega) \tag{3.3}$$

Combining this two equations we get

$$D(\omega) = \varepsilon_0 E(\omega) (1 + \chi(\omega)) \tag{3.4}$$

where χ is the electric susceptibility which measures how easily it is polarized in response to an applied electric field, and it is a dimensionless quantity.

Finally the relation between the the permittivity and susceptibility is

$$\varepsilon(\omega) = \varepsilon_0 (1 + \chi(\omega)) \tag{3.5}$$

So the relative permittivity will be

$$\varepsilon_r(\omega) = 1 + \chi(\omega) \tag{3.6}$$

For linear isotropic materials such as glass this above values become simple. But for a dispersive material, the frequency dependent permittivity and susceptibility should be modeled perfectly for getting the perfect response of the material for certain electromagnetic excitation. Some widely used material models are Drude model, Lorentz model, Debye model and Lorentz-Drude model.

3.2 Different Material Models

3.2.1 The Drude Model

The Drude model of electrical conduction was first developed by Paul Drude. In his model he described the metal as a volume filled with stationary positive ions, immersed in a gas of electrons following the kinetic theory of gases. These electrons are free to move inside the metal without any interaction with each other. The electrons in a metal are subjected to two forces, such as

1. Driving force F_d
2. Damping force F_g

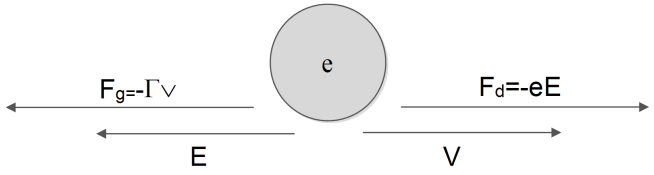

FIGURE 3.1: Drude model.

The driving force and the damping force can be expressed as

$$F_d = qE = -eE \tag{3.7}$$

$$F_g = -\Gamma v \tag{3.8}$$

As the two forces are opposite to each other, the resultant force will be

$$F = F_d - F_g \tag{3.9}$$

From Newton's first law of motion we can write

$$mr'' = -eE + \Gamma r' \tag{3.10}$$

where,

m is the mass of an electron
Γ is the damping constant in Newton second per meter
r is the displacement in meter
v is the velocity of the electron
q is the electrons charge
the prime indicates differentiation order with respect to time

For time harmonic electric field and time harmonic displacement the equation will be

$$E(t) = E_0 e^{-j\omega t} \Leftrightarrow E(\omega) \tag{3.11}$$

$$r(t) = R_0 e^{-j\omega t} \Leftrightarrow R(\omega) \tag{3.12}$$

From equaion 3.10 the frequency domain form will be

$$mR''(\omega) - \Gamma m R'(\omega) + eE(\omega) = 0 \tag{3.13}$$

The derivatives of frequency domain will give

$$-m\omega^2 R''(\omega) + j\omega\Gamma m R'(\omega) + eE(\omega) = 0 \tag{3.14}$$

Simplifying the above equation, the displacement R will give

$$R(\omega) = \frac{-e}{m(j\Gamma\omega - \omega^2)} E(\omega) \tag{3.15}$$

The polarization for n number of electrons will be

$$P(\omega) = -neR(\omega) \tag{3.16}$$

or

$$P(\omega) = \frac{ne^2}{m(j\Gamma\omega - \omega^2)} E(\omega) \tag{3.17}$$

An expression for the susceptibility can also be obtained from the above equation and that will be

$$\frac{P(\omega)}{\varepsilon_0 E(\omega)} = \frac{ne^2}{\varepsilon_0 m(j\Gamma\omega - \omega^2)} = \chi(\omega) \tag{3.18}$$

Now substituting this value in equation 3.6 we get

$$\varepsilon_r(\omega) = 1 + \frac{ne^2}{\varepsilon_0 m(j\Gamma\omega - \omega^2)} \tag{3.19}$$

if we consider ω_p as the plasma frequency that will provide

$$\omega_p^2 = \frac{ne^2}{\varepsilon_0 m} \tag{3.20}$$

So, the frequency dependent flux density will be

$$D(\omega) = \varepsilon_0 \left(1 + \frac{\omega_p^2}{j\Gamma\omega - \omega^2}\right) E(\omega) \tag{3.21}$$

For low frequency, the term $\Gamma\omega << 1$, therefore, the dispersive relation can be reduced to

$$D(\omega) = \varepsilon_0 \left(1 - \frac{\omega_p^2}{\omega^2}\right) E(\omega) \tag{3.22}$$

3.2.2 The Lorentz Model

The Lorentz model gives a simpler picture of the atom. The model is a very useful tool to visualize atom-field interaction. In this model, Lorentz modeled an atom as a mass (nucleus) connected to another smaller mass (electron). However, electrons

in the Lorentz model do not move freely inside the metal instead, they are bound to atoms. So, there is a restoring force acting between them which can be denoted by F_r

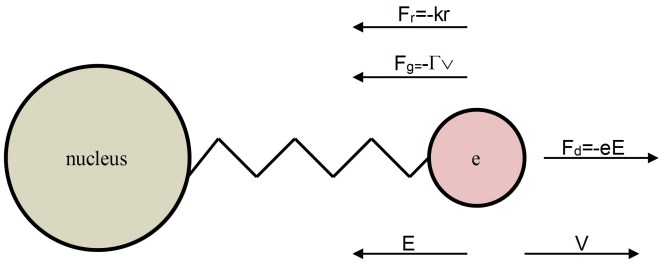

FIGURE 3.2: Lorentz model.

The restoring force can be written as

$$F_r = -kr \tag{3.23}$$

where k is the spring constant in Newtons per meter.

Similarly from the law of motion we can say that

$$mr'' + m\Gamma r' + mkr + eE = 0 \tag{3.24}$$

In frequency domain the above equation will be

$$R(\omega)\left(m\omega_0^2 + j\omega m\Gamma - m\omega^2\right) - eE(\omega) \tag{3.25}$$

Considering the natural frequency $\omega_0 = \sqrt{\frac{k}{m}}$ we get

$$R(\omega) = \frac{-e}{m\left(\omega_0^2 + j\Gamma\omega - \omega^2\right)} E(\omega) \tag{3.26}$$

Therefore the susceptibility can be found as

$$\frac{P(\omega)}{\varepsilon_0 E\omega} = \frac{ne^2}{\varepsilon_0 m\left(\omega_0^2 + j\Gamma\omega - \omega^2\right)} = \chi(\omega) \tag{3.27}$$

So from the equation 3.4 the expression for D can be expressed in frequency domain as

$$D(\omega) = \varepsilon_0 \left(1 + \frac{\omega_p^2}{\omega_0^2 + j\Gamma\omega - \omega^2}\right) E(\omega) \tag{3.28}$$

3.2.3 The Lorentz-Drude Model

In the Lorentz-Drude (LD) model, which is the most general form when an EM field is applied to a metal, the electrons of two types oscillate inside the metal, and they contribute to the permittivity. The free electrons contribute a permittivity of the Drude model, and the bound electrons contribute a permittivity of the Lorentz model. The permittivity in the LD model is given by

$$\varepsilon = \varepsilon_{free} + \varepsilon_{bound} \tag{3.29}$$

where

$$\varepsilon_{free} = 1 + \frac{\omega_p}{j\Gamma\omega - \omega^2} \tag{3.30}$$

$$\varepsilon_{bound} = \frac{\omega_p}{\omega_0 + j\Gamma\omega - \omega^2} \tag{3.31}$$

Therefore combining both the model together the electric field density D in frequency domain will be

$$D(\omega) = \varepsilon_0 \left(1 + \frac{\omega_p}{j\Gamma\omega - \omega^2} + \frac{\omega_p}{\omega_0 + j\Gamma\omega - \omega^2}\right) E(\omega) \tag{3.32}$$

The above relation is known as the Lorentz-Drude model.

3.2.4 The Debye Model

The Debye model was first developed by Peter Debye in the year 1912. According to the Debye model,materials are made of electric dipoles, so that, when an electric field is applied, these dipoles follow the behavior of the applied field with some relaxation time. If the electric field is oscillating at a slow frequency, then the polarization will be strong. On the other hand, a fast oscillating field means low polarization. From another point of view, materials with long relaxation times have low polarization or no polarization at all, and materials with short relaxation times have strong polarization. Metals are known to have very short relaxation times. Thus, polarization in metals is strong. If a DC electric field is applied to a dielectric, the polarization takes some time to follow the electric field. At steady state, it will be

$$P(t) = P_\infty \left(1 - e^{-t/\tau}\right) \tag{3.33}$$

where $P(t)$ is the instantaneous polarization,

P_∞ is the polarization in the steady state τ is the time constant.

The derivative of the above equation will be

$$\frac{dP(t)}{dt} = \frac{1}{\tau} P_\infty e^{-t/\tau} \tag{3.34}$$

Now combining both the equations we get

$$P(t) = P_\infty - \tau \frac{dP(t)}{dt} \tag{3.35}$$

As $P_\infty = \varepsilon_0 (\varepsilon - 1) E(t)$ so the equation will be reduced to

$$P(t) = \varepsilon_0 (\varepsilon - 1) E(t) - \tau \frac{dP(t)}{dt} \tag{3.36}$$

or,

$$\varepsilon_0 (\varepsilon - 1) E(t) = P(t) + \tau \frac{dP(t)}{dt} \tag{3.37}$$

In frequency domain the equation will be

$$\varepsilon_0 (\varepsilon - 1) E(\omega) = P(\omega) + j\omega\tau P(\omega) \tag{3.38}$$

or,

$$P(\omega) = \frac{\varepsilon_0 (\varepsilon - 1)}{1 + j\omega\tau} E(\omega) \tag{3.39}$$

The susceptibility can be expressed as

$$\frac{(\varepsilon - 1)}{(1 + j\omega\tau)} = \frac{P(\omega)}{\varepsilon_0 E(\omega)} = \chi(\omega) \tag{3.40}$$

The relative permittivity will be

$$\varepsilon_r(\omega) = \chi(\omega) + 1 = \frac{(\varepsilon - 1)}{(1 + j\omega\tau)} + 1 \tag{3.41}$$

For the permittivity function to fit in the range from 0 frequency to infinity frequency,the boundary conditions are $\varepsilon_r(0) = \varepsilon_s$ and $\varepsilon_r(\infty) = \varepsilon_\infty$

Therefore, the relation can be modified to

$$\varepsilon(\omega) = \varepsilon_\infty + \frac{(\varepsilon_s - \varepsilon_\infty)}{(1 + j\omega\tau)} \tag{3.42}$$

To take into account the material losses that SPPs encounter, another term is added with the permittivity of metal. So the above equation can be expanded to

$$\varepsilon(\omega) = \varepsilon_\infty + \frac{(\varepsilon_s - \varepsilon_\infty)}{(1 + j\omega\tau)} - j\frac{\sigma}{\omega\varepsilon_0} \tag{3.43}$$

The Debye model can also be expressed in real and imaginary terms

$$\varepsilon_r(\omega) = \varepsilon'(\omega) - j\varepsilon''(\omega) \tag{3.44}$$

where

$$\varepsilon'(\omega) = \varepsilon_\infty + \frac{(\varepsilon_s - \varepsilon_\infty)}{(1 + \omega^2\tau^2)} \tag{3.45}$$

and

$$\varepsilon''(\omega) = \varepsilon_\infty + \frac{(\varepsilon_s - \varepsilon_\infty)\omega\tau}{(1 + \omega^2\tau^2)} + \frac{\sigma}{\omega\varepsilon_0} \tag{3.46}$$

3.3 Material Dispersion

Dispersion can be defined as the variation of the propagating waves wavelength with frequency. It is also sometimes defined as the variation of propagating waves wave number $k = \frac{2\pi}{\lambda}$with angular frequency$\omega = 2\pi f$. So the one dimensional wave equation will be

$$\frac{\partial^2 u}{\partial t^2} = v^2 \frac{\partial^2 u}{\partial x^2} \tag{3.47}$$

where

$v^2 = \frac{1}{\mu\varepsilon}$ The solution of the above wave equation can be written in phasor form as

$$u(x,t) = e^{j(\omega t - kx)} \tag{3.48}$$

Now putting this value in the wave equation we get

$$(j\omega)^2 e^{j(\omega t - kx)} = v^2(-jk)^2 e^{j(\omega t - kx)} \tag{3.49}$$

Finally from this equation we get

$$k = \pm\frac{\omega}{v} \tag{3.50}$$

The + sign is for -x directed wave propagation and - sign is for +x directed wave propagation. The magnetic flux density and electric flux density for dispersive medium are

$$D(\omega) = \varepsilon(\omega) E \tag{3.51}$$

$$B(\omega) = \mu(\omega) H \tag{3.52}$$

Here both $\varepsilon(\omega)$ and $\mu(\omega)$ are frequency dependent functions.

Chapter 4

Overview of Finite-Difference Time-Domain Method

4.1 The Yee Algorithm

The algorithm used in FDTD simulations is known as the Yee algorithm. The original proposal was intended for homogeneous, isotropic and lossless media based on discretizing the volume into cells in Cartesian coordinates. The Yee algorithm solves for both electric and magnetic fields using the coupled Maxwell's time-dependent curl equations, rather than solving for the electric field alone (or the magnetic field alone) with a wave equation.
The method begins with two of Maxwell's equations:

$$D\frac{\partial \overrightarrow{H}}{\partial t} = -\frac{1}{\mu}\nabla \times \overrightarrow{E} \tag{4.1}$$

$$D\frac{\partial \overrightarrow{E}}{\partial t} = \frac{1}{\varepsilon}\nabla \times \overrightarrow{H} \tag{4.2}$$

The electric and magnetic fields are three dimensional vectors. Each equation can be converted into three coupled scalar first order differential equations. The derivatives are both in space and time. The curl operations of equations 4.1 and equation 4.2 yields the following six equations in Cartesian coordinates

$$\frac{\partial E_z}{\partial y} - \frac{\partial E_y}{\partial z} = \mu\frac{\partial H_x}{\partial t} \tag{4.3}$$

$$\frac{\partial E_x}{\partial z} - \frac{\partial E_z}{\partial x} = \mu \frac{\partial H_y}{\partial t} \tag{4.4}$$

$$\frac{\partial E_y}{\partial x} - \frac{\partial E_x}{\partial y} = \mu \frac{\partial H_z}{\partial t} \tag{4.5}$$

$$\frac{\partial H_z}{\partial y} - \frac{\partial H_y}{\partial z} = \varepsilon \frac{\partial E_x}{\partial t} \tag{4.6}$$

$$\frac{\partial H_x}{\partial z} - \frac{\partial H_z}{\partial x} = \varepsilon \frac{\partial E_y}{\partial t} \tag{4.7}$$

$$\frac{\partial H_y}{\partial x} - \frac{\partial H_y}{\partial y} = \varepsilon \frac{\partial E_z}{\partial t} \tag{4.8}$$

Then the scalar differential equations are converted into difference equations. In order to do that, discretization is required for both space and time. For space discretization, Yee visualized the field components arranged within a unit cell (voxel). The electric field components are stored on the corresponding cell edges, while the magnetic field components are stored on the corresponding face centers. The fields are located in a way where each E component is surrounded by four H components and vice versa, which leads to a spatially coupled system of field circulations corresponding to the law of Faraday and Ampere. The figure 4.1 shows the Yee's spatial grid.

Considering a two dimensional TM(Transverse Magnetic) polarized field case,

$$\frac{\partial E_x}{\partial t} = \frac{1}{\varepsilon} \frac{\partial H_z}{\partial y} \tag{4.9}$$

$$\frac{\partial E_y}{\partial t} = \frac{1}{\varepsilon} \frac{\partial H_z}{\partial x} \tag{4.10}$$

$$\frac{\partial H_z}{\partial t} = \frac{1}{\mu} \left(\frac{\partial E_x}{\partial y} - \frac{\partial H_y}{\partial x} \right) \tag{4.11}$$

Central difference approximation is applied in each of the equations 4.9, 4.10 and 4.11 which finally conclude in a spatial scalar difference equations in 4.12, 4.13 and 4.14.

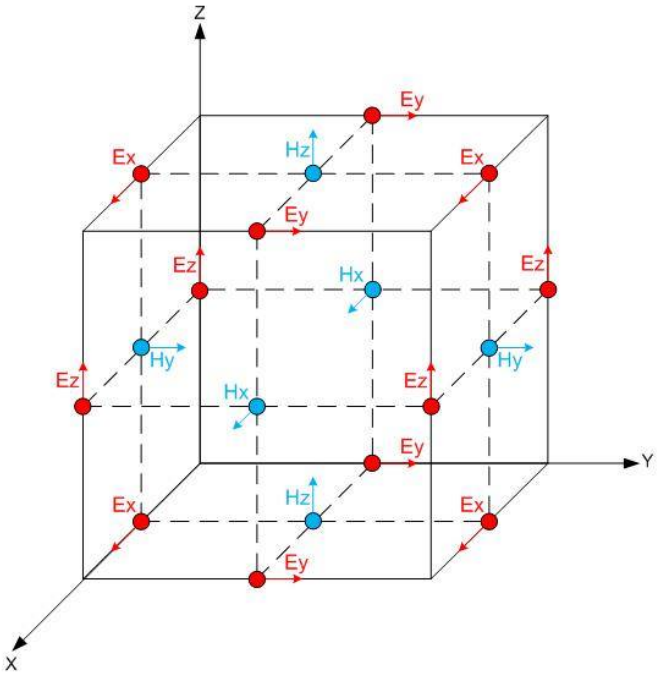

FIGURE 4.1: Yee's spatial grid.

$$\frac{\partial E_x}{\partial t} = \frac{1}{\varepsilon}\frac{H_z\left(i,j\right) - H_z\left(i,j-1\right)}{\Delta y} \tag{4.12}$$

$$\frac{\partial E_y}{\partial t} = \frac{1}{\varepsilon}\frac{H_z\left(i,j\right) - H_z\left(i-1,j\right)}{\Delta x} \tag{4.13}$$

$$\frac{\partial H_z}{\partial t} = \frac{1}{\mu}\left(\frac{E_x\left(i,j+1\right) - E_x\left(i,j\right)}{\Delta y} - \frac{E_y\left(i+1,j\right) - E_y\left(i,j\right)}{\Delta x}\right) \tag{4.14}$$

In order to consider the time derivatives, the time axis is to be considered as shown in the figure. The Electric and Magnetic field are mapped half a step apart along the time axis. Again applying the central difference approximation the equations 4.12, 4.13 and 4.14 become:

$$\frac{E_x^{n+1}\left(i+\frac{1}{2},j\right) - E_x^{n}\left(i+\frac{1}{2},j\right)}{\Delta t} = \frac{1}{\varepsilon}\frac{H_z^{n+\frac{1}{2}}\left(i+\frac{1}{2},j\right) - H_z^{n+\frac{1}{2}}\left(i+\frac{1}{2},j-\frac{1}{2}\right)}{\Delta y}$$

$$\frac{E_y^{n+1}\left(i,j+\frac{1}{2}\right) - E_y^{n}\left(i,j+\frac{1}{2}\right)}{\Delta t} = -\frac{1}{\varepsilon}\frac{H_z^{n+\frac{1}{2}}\left(i+\frac{1}{2},j+\frac{1}{2}\right) - H_z^{n+\frac{1}{2}}\left(i-\frac{1}{2},j+\frac{1}{2}\right)}{\Delta y}$$

$$\frac{H_z^{n+\frac{1}{2}}\left(i+\frac{1}{2},j+\frac{1}{2}\right)-H_z^{n-\frac{1}{2}}\left(i+\frac{1}{2},j+\frac{1}{2}\right)}{\Delta t}=-\frac{1}{\mu}\left(\frac{E_x^{n+1}\left(i+\frac{1}{2},j+1\right)-E_x^{n}\left(i+\frac{1}{2},j\right)}{\Delta y}-\right.$$

$$\left.\frac{E_y^{n}\left(i+1,j+\frac{1}{2}\right)-E_y^{n}\left(i,j+\frac{1}{2}\right)}{\Delta x}\right)$$

Each field component depends on the field of previous time step itself and the surrounding component in Yee's algorithm.

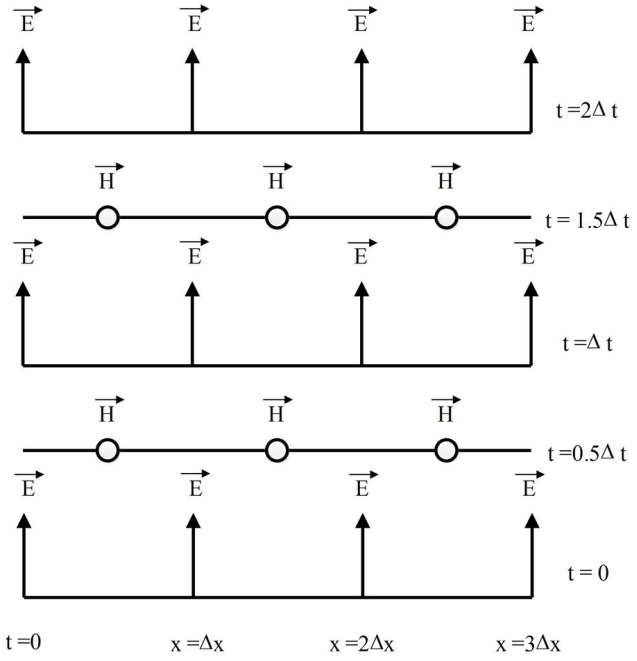

FIGURE 4.2: The temporal scheme of FDTD method.

Numerical stability of the Yee algorithm is required to be ensured. In an unstable algorithm the computed magnitude of electric and magnetic field components will gradually increase without limit with the progression of simulation. To guarantee numerical stability, the EM field's propagation should not be faster than the allowed limit which is imposed by the phase velocity within the material. This is done by limiting time step Δt using the Courant-Friedrichs-Lewy criterion for the general Yee FDTD grid as follows:

$$\Delta t \leq \left\{ \frac{1}{v_p \cdot \sqrt{\frac{1}{(\Delta x)^2}+\frac{1}{(\Delta y)^2}+\frac{1}{(\Delta z)^2}}} \right\} \tag{4.15}$$

where Δx, Δy and Δz indicate the spatial Cartesian grid increments.

4.2 Absorbing Boundary Condition (ABC)

In FDTD method, a space of theoretically infinite extent with a finite computational cell is simulated due to limited computer resources. The boundary is said to be ideally absorbing, without any non-physical reflection back to the region. To accomplish this, a number of boundary conditions such as Berenger's perfectly matched layer (PML), have been proposed. An artificial layer surrounds the computational domain so that most of the outgoing waves are absorbed. The electromagnetic fields are made to attenuate rapidly until they become equal to zero, so that they do not produce any reflections.

4.3 Material Dispersion in FDTD

The material is said to be dispersive when the permittivity and permeability of a material are functions of frequency. In reality the assumption of constant relative permittivity is not absolutely correct. Because by doing so, instantaneous polarization of charge within a material is being assumed. In order to exploit the realistic wave propagation, dispersive FDTD techniques become necessary. The existing FDTD based algorithms for the analysis of material dispersion can be categorized into three types:

1) the auxiliary differential equation (ADE),
2) the Z-transform methods, and
3) methods base on discrete convolution of the dispersion relation or the recursive convolution (RC) method [33].

We will highlight on the ADE dispersive FDTD method as we have applied in material modeling. The other methods will also be briefly discussed.

4.3.1 The Auxiliary Differential Equation(ADE)

Taflove introduced the auxiliary differential equation to the FDTD modeling in order to integrate the dispersion relation into the model. The dispersion relation is converted from frequency domain to time domain through Fourier transform in the basic step of the procedure. The Fourier transform results in a relationship between the new E field value and the previous E and D values, which can be

added to the algorithm to update the E fields. The new algorithm with ADE becomes

$$\frac{\partial}{\partial t}H_z = -\frac{1}{\mu}\left(\frac{\partial E_x}{\partial y} - \frac{\partial E_y}{\partial x}\right) \tag{4.16}$$

$$\frac{\partial}{\partial t}D_x = \left(\frac{\partial H_z}{\partial y}\right) \tag{4.17}$$

In order to get the function relating D to E in a dispersive medium, we start with

$$D(\omega) = \varepsilon_o \frac{\sigma}{j\omega} E(\omega) \tag{4.18}$$

Multiplying by $j\omega$

$$j\omega D(\omega) = \varepsilon_o \sigma E(\omega) \tag{4.19}$$

Applying the Fourier transform in equation 4.19

$$\frac{d}{dt}D(t) = \varepsilon_o \sigma E(t) \tag{4.20}$$

Discretizing equation 4.20 equation using forward difference method

$$\frac{D^n - D^{n-1}}{\Delta t} = \varepsilon_o \sigma E(t) \tag{4.21}$$

Finally solving for E, we find the update equation

$$E^n = \frac{D^n - D^{n-1}}{\varepsilon_o \sigma \Delta t} \tag{4.22}$$

4.3.2 The Z-transform Methods

The Z-transform is a faster method compared to ADE method. Sullivan used the Z-transform method for the first time in order to introduce the dispersion relation into the FDTD algorithm.

The Z-transform of the equation

$$D(\omega) = \varepsilon(\omega) E(\omega) \tag{4.23}$$

is

$$D(z) = \varepsilon(z) \Delta t E(z) \tag{4.24}$$

where $\varepsilon(z)$ is the z-transform of $\varepsilon(\omega)$ and is the sampling period. As already done in ODE, let us consider the material dispersion as $\frac{\sigma}{j\omega}$, the relation between D and E is given by

$$D(\omega) = \frac{\varepsilon_o \sigma}{1 - z^{-1}} \Delta t E(z) \tag{4.25}$$

Multiplying by $(1 - z^{-1})$, we find

$$D(z)\left(1 - z^{-1}\right) = \varepsilon_o \sigma E(z) \tag{4.26}$$

or,

$$D(z) - z^{-1} D(z) = \varepsilon_o \sigma E(z) \tag{4.27}$$

Performing inverse z-transform

$$D^n - D^{n-1} = \varepsilon_o \sigma \Delta t E^n \tag{4.28}$$

Finally, for solving E from equation 4.28, we find

$$E^n = \frac{D^n - D^{n-1}}{\varepsilon_o \sigma \Delta t} \tag{4.29}$$

which is same as the final update equation derived by ADE method.

4.3.3 Piecewise Linear Recursive Convolution Method

Luebbers et al. formulated the first frequency dispersive FDTD algorithm using the recursive convolution (RC) scheme. Later it became piecewise linear recursive convolution(PLRC) method [34]. Initially developed for Debye media [33], the approach was later extended for the study of wave propagation in a Drude material [35], N-th order dispersive media [36], an anisotropic magneto-active plasma [37], ferrite material [38] and the bi-isotropic/chiral media [39] [40] [41].
The RC approach, typically being faster and having required fewer computer memory resources than other approaches, is usually less accurate. But in case of multiple pole mediums, it is easier to follow the RC approach.
In the initial derivation of PLRC method for a linear dispersive medium, the relation between electric flux density and electric field intensity is expressed as:

$$D(t) = \varepsilon_o \varepsilon_\infty E(t) + \varepsilon_o \int_0^t E(t-\tau)\,\chi(\tau) d\tau \tag{4.30}$$

which can be discretized as:

$$D^n = \varepsilon_o \varepsilon_\infty E^n + \varepsilon_o \int_0^{n\Delta t} E(n\Delta t - \tau)\,\chi(\tau) d\tau \tag{4.31}$$

The PRC method is further preceded from this basing discrete equation.

4.3.4 The General Algorithm

The derivation of equations for multi-pole dispersion relation is more difficult compared to the single pole-pair dispersion relation. For example, for six-pole Lorentz-Drude dispersion the required derivation process is lengthy. Additionally, the memory required for computation is also vast. There are various methods proposed by researchers regarding this topic such as Taflove's matrix inversion method, Multi-term dispersion by Okoniewski, etc. However Alsunaidi and Al-Jabr proposed a general algorithm technique which solves various problems regarding previous methods. The major advantage of this technique is that it requires only one algorithm for anyt dispersion relation. The dispersive relation has the general form as

$$D(\omega) = \varepsilon(\omega) E(\omega) \tag{4.32}$$

which can be expressed in terms of summation of poles

$$D(\omega) = \varepsilon_o \varepsilon_\infty E(\omega) + \sum_i^N P_i(\omega) \tag{4.33}$$

where N is the number of poles. Applying Fourier transform, this equation becomes

$$D^{n+1} = \varepsilon_o \varepsilon_\infty E^{n+1} + \sum_i^N P_i{}^{n+1} \tag{4.34}$$

or,

$$E^{n+1} = \frac{D^{n+1} - \sum_i^N P_i{}^{n+1}}{\varepsilon_o \varepsilon_\infty} \tag{4.35}$$

This term P_i can be any form of dispersion relation such as the Debye, the Drude or just the conductivity term. This the final solved equation for E.

Chapter 5

Parameter Extraction of Optical Materials

The Modified Debye Model (MDM) parameters for five metals are presented. A nonlinear optimization algorithm has been developed in order to extract the parameters for the metals. The extracted parameters have been used to determine the complex relative permittivity of the metals in optical and near-IR region of electromagnetic spectrum. The obtained results have been compared with the experimental values and an excellent agreement has been found.

5.1 Material Models

5.1.1 Modified Debye Model

5.1.1.1 Metals

The complex relative permittivity function of the modified Debye model is described by the following equation,

$$\varepsilon_r(\omega) = \varepsilon_\infty + \frac{\varepsilon_s - \varepsilon_\infty}{(1 + j\omega\tau)} - j\frac{\sigma}{\omega\varepsilon_o} \tag{5.1}$$

where, ε_∞ is the infinite frequency relative permittivity, ε_s is the zero frequency relative permittivity, ω is the angular frequency, σ is the conductivity and τ is the relaxation time.

If the model is represented in terms of its real and imaginary parts, then,

$$\varepsilon_r(\omega) = \varepsilon'(\omega) - j\varepsilon''(\omega) \tag{5.2}$$

where, the real part of the complex relative permittivity is, $\varepsilon'(\omega) = \varepsilon_\infty + \frac{\varepsilon_s - \varepsilon_\infty}{(1+\omega^2\tau^2)}$ and the imaginary part of the complex relative permittivity is, $\varepsilon''(\omega) = \frac{(\varepsilon_s - \varepsilon_\infty)\omega\tau}{(1+\omega^2\tau^2)} + \frac{\sigma}{\omega\varepsilon_o}$

From equation 5.1, we can see that the modified Debye model can be described by four parameters which are ε_∞, ε_s, σ and τ. However, a relationship can be derived among these parameters by comparing equation 5.1 with the Drude model equation as,

$$\sigma = \varepsilon_o(\varepsilon_\infty - \varepsilon_s)/\tau \tag{5.3}$$

Now we actually have three parameters that need to be extracted and the other can be obtained from equation 5.3.

5.1.1.2 Dielectric Materials

The frequency dependent permittivity function of Modified Debye Model is given by,

$$\varepsilon_r(\omega) = \varepsilon_\infty + \frac{\varepsilon_s - \varepsilon_\infty}{(1 + j\omega\tau)} \tag{5.4}$$

where, ε_∞ is the infinite frequency relative permittivity, ε_s is the zero frequency relative permittivity, ω is the angular frequency and τ is the relaxation time.

From equation 5.4 we can see that modified Debye model for dielectric material can be described by three parameters which are ε_∞, ε_s and τ.These three parameters need to be optimized in order to model dielectric materials using MDM.

5.1.2 Lorentz Model

The frequency dependent complex permittivity function for single pole-pair Lorentz model is given by

$$\varepsilon_r(\omega) = \varepsilon_\infty + \frac{{\omega_o}^2(\varepsilon_s - \varepsilon_\infty)}{{\omega_o}^2 + j2\delta\omega - \omega^2} \tag{5.5}$$

where, ε_∞ is the infinite frequency relative permittivity, ε_s is the zero frequency relative permittivity, ω_o is the frequency of the pole pair and δ is the damping frequency.

From equation 5.5, it can be observed that single pole-pair Lorentz model can be described by four parameters which are ε_∞, ε_s, ω_o and δ. These four parameters are independent and need to be extracted.

5.2 Method Of Optimization

The algorithm that we have used is as follows. First we obtain the experimental values from the book of Palik [42] and use them to obtain the complex relative permittivity for each material. Then the program varies the three parameters that need to be extracted and try different combinations to obtain the complex relative permittivity. The square of the complex relative permittivity obtained using the extracted parameters are subtracted from the square of the complex relative permittivity obtained using experimental values. The squared differential term is then compared with a predetermined tolerance value which is near to zero and the iteration goes on until the preset value is reached. The variation in the modeling parameters is random; however, boundary limits have been set so that the extracted parameters meet the requirement of the FDTD method. Varying the modeling parameters in a random fashion is the most challenging part of the algorithm. If a linear method was used to vary the parameters, the computation time would have been much higher. Since the variation is random, it takes less time to find a combination of values that produces the least squared difference.

The boundary conditions that need to be maintained for the MDM parameters to be integrated in the FDTD algorithm are $\varepsilon_\infty > 1$, $\varepsilon_s < \varepsilon_\infty$ and $\sigma \geq \varepsilon_o(\varepsilon_\infty - \varepsilon_s)/\tau$.

The flow chart of the optimization algorithm is given in figure 5.1. The algorithm has been developed solely for single pole-pair modeling parameter extraction. The accuracy of the obtained results reduces significantly if the modeling parameters for more complex curves are extracted using this optimization algorithm.

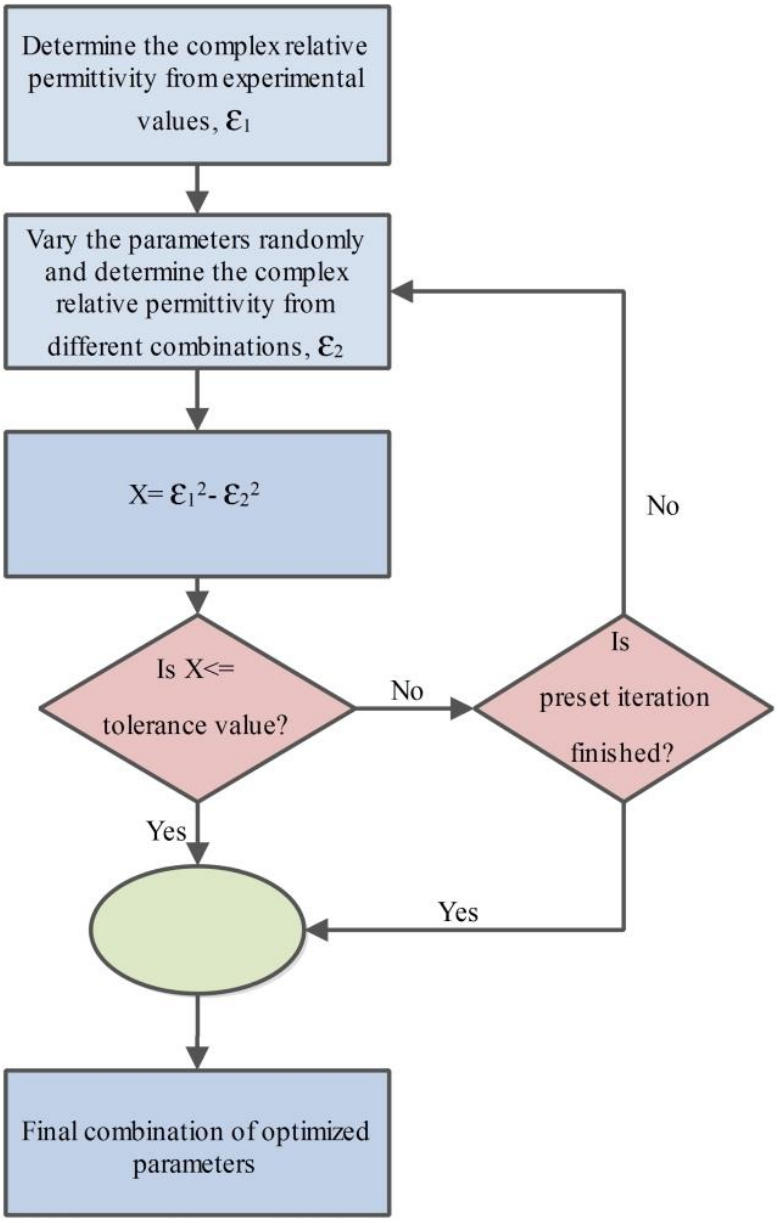

FIGURE 5.1: Flow chart of the optimization algorithm.

5.3 Extracted Parameters

5.3.1 Metals

TABLE 5.1: Extracted Parameters for Five Metals for modified Debye model

Parameters	**Nickel**	**Hexagonal Cobalt**	**Palladium**	**Iridium**	**Titanium**
ε_∞	2.2986	1.0001	1.001	1.0001	7.59
ε_s	-22.52	-25.65	-22	-40.92	-11.99
$\sigma(S/m)$	6.74×10^5	7.86×10^5	7.53×10^5	1.01×10^6	6.21×10^5
$\tau(sec)$	3.26×10^{-16}	3×10^{-16}	2.7×10^{-16}	3.7×10^{-16}	2.79×10^{-16}
Range of Wavelength(nm)	$600 - 1100$	$350 - 1000$	$300 - 700$	$600 - 1100$	$400 - 700$
RMS Deviation	1.027	1.1510	0.2489	1.6216	1.1239

The extracted parameters for the five metals using our developed algorithm are presented in table 5.1. From the table it can be observed that a maximum RMS deviation of 1.62 occurs for Iridium which indicates the robustness and accuracy of our optimization algorithm.

The complex relative permittivity for each metal has been determined using both extracted parameters and experimental values. Then the real and imaginary parts have been separated from the complex relative permittivity and plotted which is presented in figures 5.2 to 5.6. The red color indicates the imaginary part while the blue color indicates the real part of the complex relative permittivity. The solid lines denote the extracted parameters and the dotted lines denote the experimental values. From the figure it is clearly visible that the real and imaginary parts of the complex relative permittivity obtained using extracted parameters agree very well with the real and imaginary parts of the complex relative permittivity obtained from the experimental values [42].

The parameters obtained by Rakic et al. [26] for Nickel exhibits an RMS deviation of 4.38 in the wavelength range of 600 to 1100 nm and the parameters obtained by Pernice et al. [25] for Nickel shows an RMS deviation of as large as 24.11 whereas our obtained parameters show an RMS deviation of only 1.02. For Palladium, the RMS deviation for the parameters reported by Rakic et al. [26] is 3.1251 while it is only 0.25 for our case within the wavelength range of 300 to 700 nm.

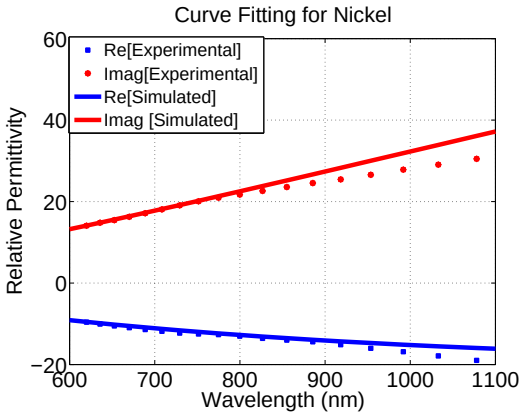

FIGURE 5.2: Curve Fitting for Nickel

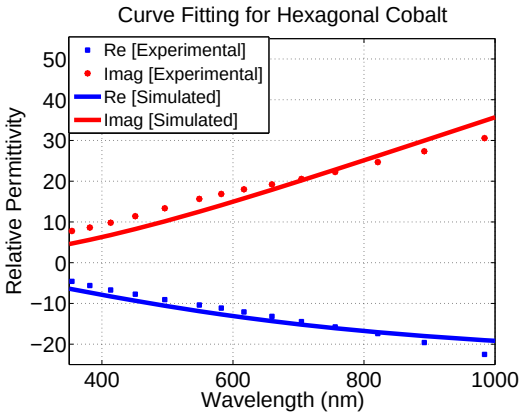

FIGURE 5.3: Curve Fitting for Hexagonal Cobalt

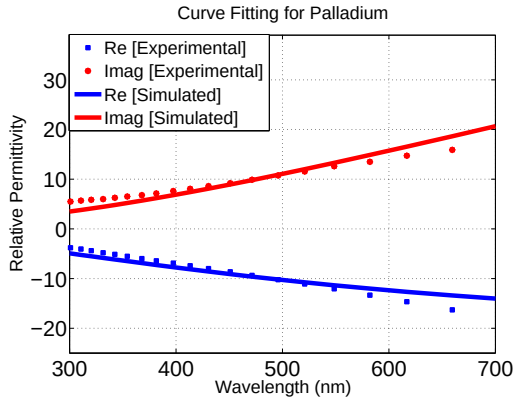

FIGURE 5.4: Curve Fitting for Palladium

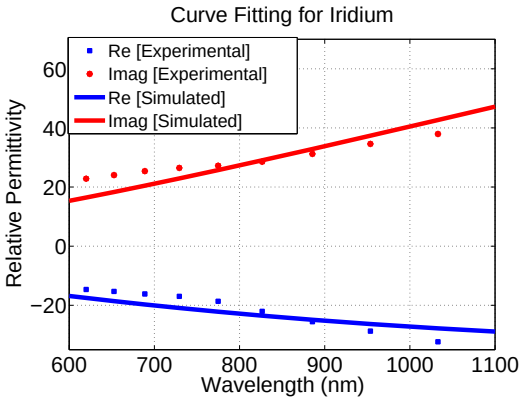

FIGURE 5.5: Curve Fitting for Iridium

The optimization method we have developed adopts random variation of the modeling parameters which reduces the computation time significantly while maintaining an excellent degree of accuracy for the single-pole material models. This is evident from the RMS deviation comparison of our extracted parameters with the results reported by other researchers.

We have utilized single pole-pair Debye model to fit our curves for the materials while Rakic et al. [26] have used a six-pole Lorentz-Drude model and Pernice et al. [25] have used a four-pole model for the fitting purpose of the frequency dependent complex permittivity curve of metals. The more is the number of poles, the higher is the computation time required. Our single pole-pair model requires significantly less computation time in comparison to multiple-pole models. We have simulated both single-pole and six-pole models for Nickel in an intel Core i5 processor based computer and found that the computation time is reduced by $\tilde{1}5\%$

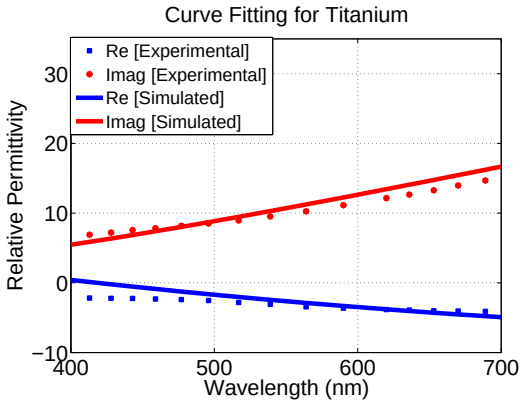

FIGURE 5.6: Curve Fitting for Titanium

using our extracted parameters. The difference in the computation time would be even more noticeable for longer distances of propagation. Therefore, it is evident that our results are better than theirs in terms of both accuracy and computation time.

5.3.2 Dielectric Materials using Modified Debye Model

TABLE 5.2: Extracted Parameters for Silicon-Germanium Alloy and Cuprous Oxide for modified Debye model

Parameters	**SiGe**	**Cuprous Oxide**
ε_∞	14.2996	6.8396
ε_s	1.519	5.819
$\tau(sec)$	2.261	4.26×10^{-15}
Range of Wavelength(nm)	$900 - 1300$	$850 - 1500$
RMS Deviation	0.3710	0.1638

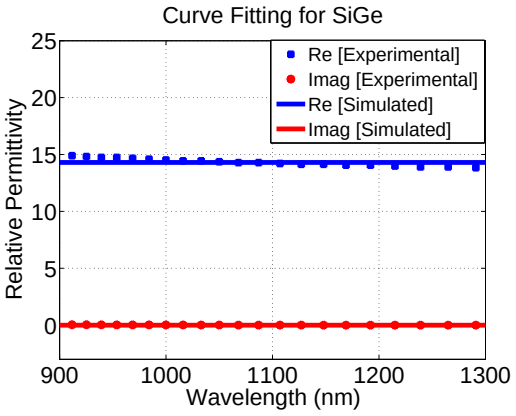

FIGURE 5.7: Curve Fitting for Silicon-Germanium Alloy using modified Debye model.

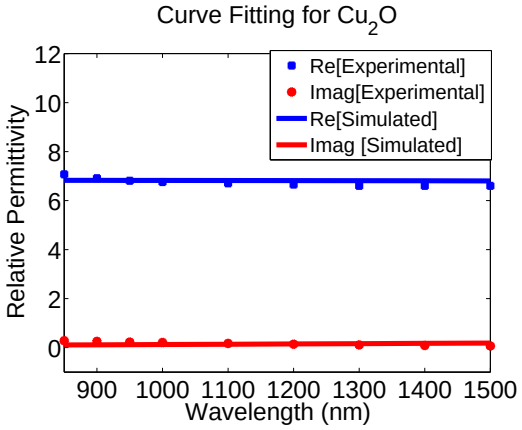

FIGURE 5.8: Curve Fitting for Cuprous Oxide using modified Debye model.

5.3.3 Dielectric Materials using Lorentz Model

The summary of our optimized parameters for single pole-pair Lorentz model and single pole-pair modified Debye model is presented in table 5.2 and table 5.3 respectively. The range of applicable wavelength and the RMS deviations are also mentioned. From the tables we can see that our parameters can be applied for a wide range of wavelengths.

The comparisons between our obtained results and the experimental values have been graphically shown in figures 5.7 and 5.8 for single pole-pair Lorentz model and

TABLE 5.3: Extracted Parameters for Silicon-Germanium Alloy and Cuprous Oxide for Lorentz model

Parameters	**SiGe**	**Cuprous Oxide**
ε_∞	1.4641	1.9881
ε_s	12.881	6.2001
$\delta(rad/s)$	7.1×10^{10}	6.1×10^{10}
$\omega_o(rad/s)$	5.3×10^{15}	0.53×10^{16}
Range of Wavelength(nm)	$900 - 1300$	$800 - 1500$
RMS Deviation	0.15	0.08

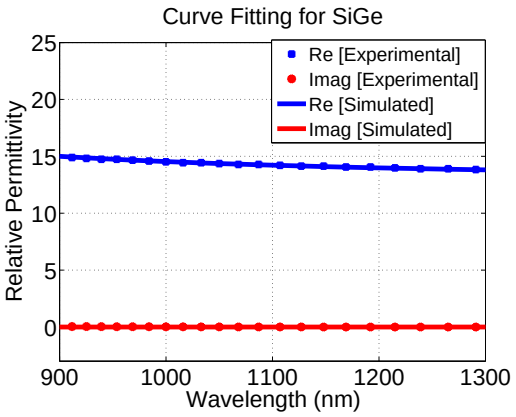

FIGURE 5.9: Curve Fitting for Silicon-Germanium Alloy using Lorentz model.

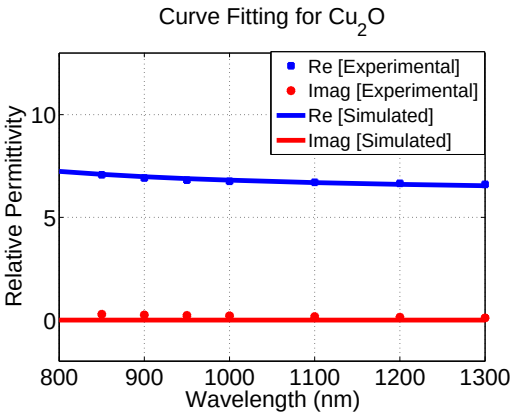

FIGURE 5.10: Curve Fitting for Cuprous Oxide using Lorentz model.

in figures 5.9 and 5.10 for single pole-pair modified Debye model. From the figures it is clearly visible that our extracted parameters agree well with the experimental results for both the material models. Therefore, our optimized parameters are valid for the range of frequency we have mentioned.

Chapter 6

Investigation of SPP Propagation in Optical Nanostructures

6.1 Developing Simulation Model

The simulation model we have developed is based on the FDTD method [43]. We have utilized the general auxiliary differential equation (ADE) based FDTD [44] approach in order to incorporate the frequency dependent dispersion property of the constituent materials. This algorithm is useful for the simulation of materials with different dispersive properties. The perfectly matched layer [45] has been integrated at all the boundaries in order to prevent back reflections.

Considering the material dispersion, the frequency-dependent electric flux density can be given as

$$D(\omega) = \varepsilon_o \varepsilon_\infty E(\omega) + P(\omega) \tag{6.1}$$

The general Lorentz model is given by

$$P(\omega) = \frac{a}{b + jc\omega - d\omega^2} E(\omega) \tag{6.2}$$

which can be written in time-domain through inverse Fourier transform as

$$bP(t) + cP'(t) + dP''(t) = aE(t) \tag{6.3}$$

The FDTD solution for the first order polarization of Eq. (3) can be expressed as

$$P^{n+1} = C_1 P^n + C_2 P^{n-1} + C_3 E^n \tag{6.4}$$

where, $C_1 = \frac{4d-2b\Delta t^2}{2d+c\Delta t}, C_2 = \frac{-2d-c\Delta t}{2d+c\Delta t}, C_3 = \frac{2a\Delta t^2}{2d+c\Delta t}$

The values of C_1, C_2 and C_3 depend on the material under consideration. Finally the electric field intensity becomes,

$$E^{n+1} = \frac{D^{n+1} - \sum_{i=1}^{N} P_i^{n+1}}{\varepsilon_o \varepsilon_\infty} \tag{6.5}$$

where, N is the number of poles and D^{n+1} is the update value of the electric flux density calculated using FDTD algorithm.

6.2 Verification of the Developed Simulation Model

In order to verify our developed simulation model we have simulated one dimensional dispersive material using the parameters given by Taflove [46]. The obtained result has been compared with the result provided by Taflove [46] and we have found an excellent agreement.The parameters given in the book of Taflove [46] are as follows, $\varepsilon_\infty = 2.25$, $\varepsilon_s = 5.25$, $\omega_o = 4 \times 10^{14}(rad/sec)$ and $\delta = 2 \times 10^9(rad/sec)$.

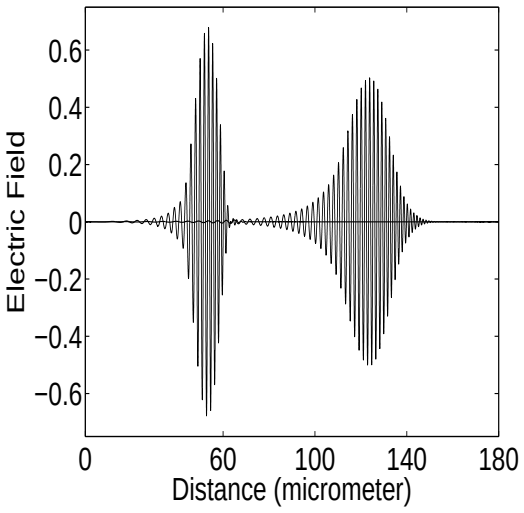

FIGURE 6.1: Simulated result using parameters given in the book of Taflove.

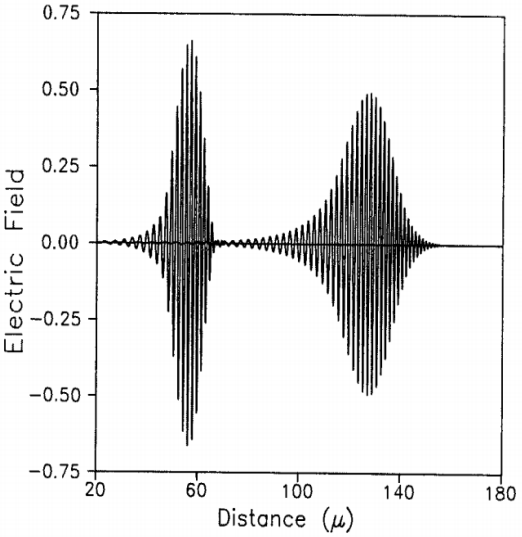

FIGURE 6.2: Result given in the book of Taflove.

6.3 SPP Propagation through Different Nanostructures

6.3.1 Metal-Dielectric-Metal Waveguide with a Combiner

We present the propagation characteristics of Surface Plasmon Polariton in the nanoscale metal-dielectric-metal waveguides which consist of a combiner. The propagation loss due to absorption by metal and reflection at the point of recombination are analyzed numerically. We have investigated the structure with different dielectric materials (air, aluminum gallium arsenide, gallium lanthanum sulfide) and for different wavelengths of the input signal. The wavelength dependent reflection coefficient, return loss and voltage standing wave ratio have also been reported in order to analyze the performance of the combiner.

The schematic diagram of the structure used for simulation is given in figure 6.3. The thickness of dielectric layer before recombination is taken as 25 nm for each section and after recombination as 70 nm. The recombination occurs at a distance of 2.3 micrometer.

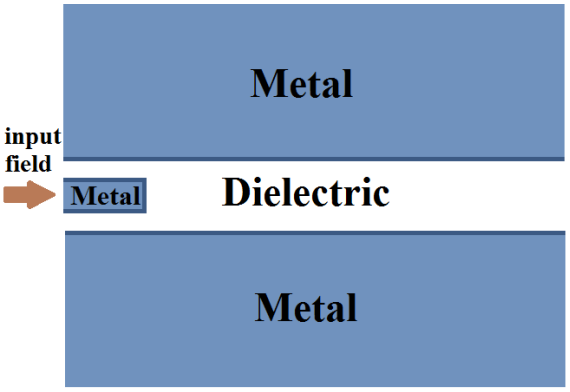

FIGURE 6.3: Schematic Diagram of the MDM waveguide with combiner used for simulation.

In order to model the metal we have used the six-pole Lorentz-Drude model. The frequency dependent permittivity function of Lorentz-Drude 6 (six) pole model is given by,

$$\varepsilon_r(\omega) = 1 - \frac{f_o\omega_p^2}{\omega^2 - j\Gamma_o\omega} + \sum_{i=1}^{5} \frac{f_i\omega_p^2}{\omega_i^2 + j\Gamma_i\omega - \omega^2} \tag{6.6}$$

where, ω_p is the plasma frequency, Γ_i is the damping frequency, f_i is the oscillator strength, j is the imaginary unit and ω_i is the resonant frequency of the i^{th} pole.

The modeling parameters for Ag that we have used, have been determined by Rakic et al. [26]. The dispersion properties for AlGaAs and GLS, have been determined by M. Alsunaidi et al. [47] and R H Sagor [48] respectively .

At the beginning, we simulated the MDM waveguide with recombination structure with the input pulse given in figure 6.4 in order to generate the SPP modes. Then we pumped the mode given in figure 6.5 into the structure modulated by a gaussian pulse having characterisitc pulse width of 3 femtoseconds and different wavelengths.

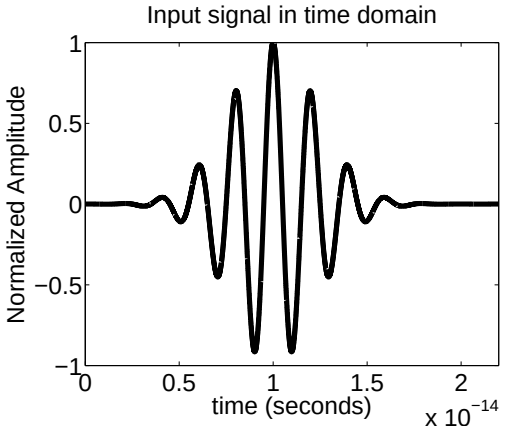

FIGURE 6.4: Input singal in time domain.

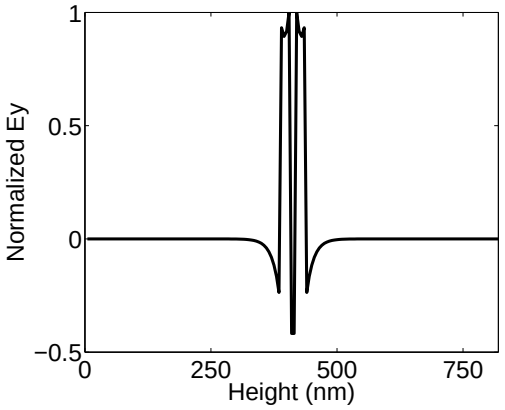

FIGURE 6.5: Ey profile pumped into the mdm waveguide with combiner.

The reflection coefficient as a function of the wavelength has been determined numerically and presented in figure 6.6. From the figure it can be observed that the reflection coefficient is the highest at 600 nm for air, 900 nm for GLS and 1200 nm for AlGaAs. At telecom wavelength the reflection coefficient for air is the lowest having a value of 0.084 whereas for AlGaAs it is 0.863.

From the numerically determined reflection coefficient, we have obtained the return loss and VSWR using analytical equations the plot of which are given in figure 6.7 and figure 6.8. At the optical communication wavelength the return loss for air is 21.5 dB whereas for GLS it is 6.74 dB and for AlGaAs it is 1.21 dB.

We simulated the MDM waveguide with combiner using the 2D FDTD simulator and obtained the electric field distribution which is given in figure 6.12. The normalized power curves for different dielectric materials and different wavelengths of the input signal are also determined and presented in figures 6.9 to 6.11. From the figure, we can observe that there is a sharp fall in the power curve at around 2.25 micrometer where the recombination occurs. This happens because of the

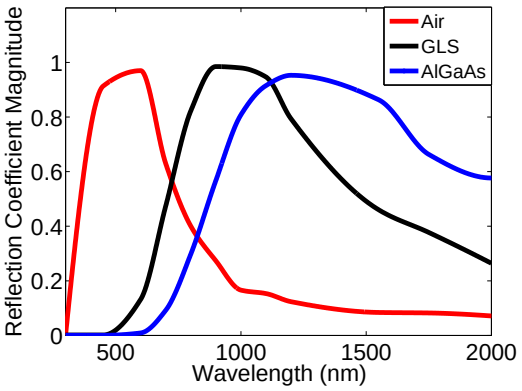

FIGURE 6.6: Reflection coefficient as a function of wavelength.

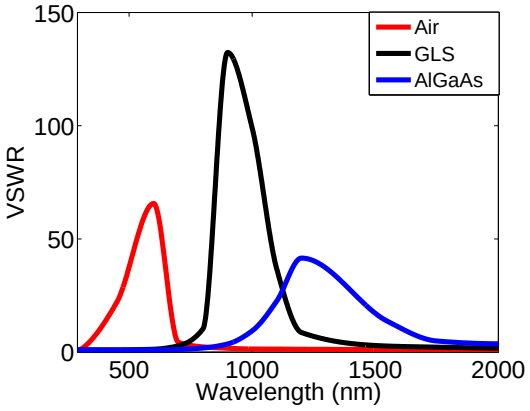

FIGURE 6.7: Voltage Standing Wave Ratio as a function of wavelength.

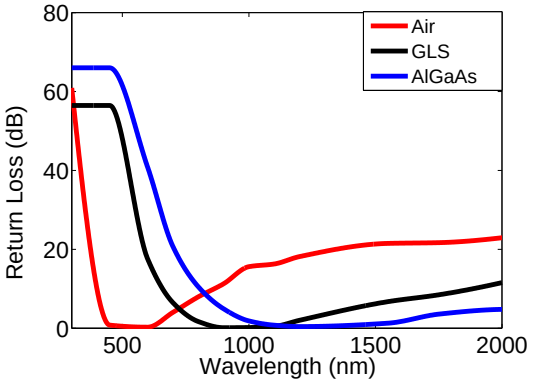

FIGURE 6.8: Return loss as a function of wavelength.

discontinuity of the metal at the point of recombination. SPPs get scattered with multiple reflection at this point which causes significant reduction in power.

The MDM waveguide constructed with air shows the least attenuation of power with distance, while the waveguide made by AlGaAs shows the highest attenuation. From the normalized power curves we can also see that propagation loss depends on the wavelength of the input signal. When the wavelength is 600 nm, the propagation length is about 12.5 micrometer for air, 1.25 micrometer for gallium lanthanum sulphide and less than 1 micrometer for aluminium gallium arsenide, but when the wavelength is increased to 1200 nm, the propagation length is extended to more than 25 micrometer for air, 10 micrometer for gallium lanthanum sulphide and 5 micrometer for aluminium gallium arsenide.

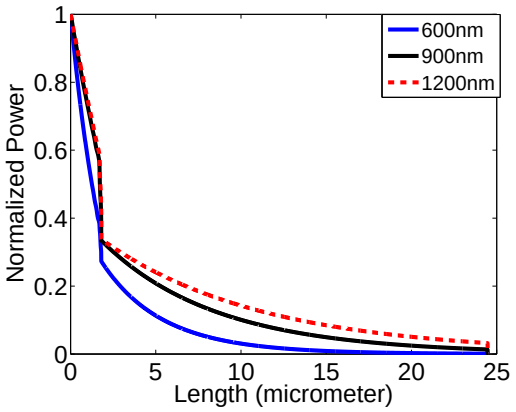

FIGURE 6.9: Normalized power curve for air.

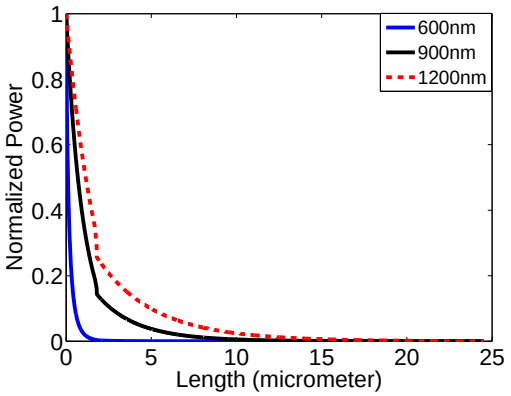

FIGURE 6.10: Normalized power curve for gallium lanthanum sulfide.

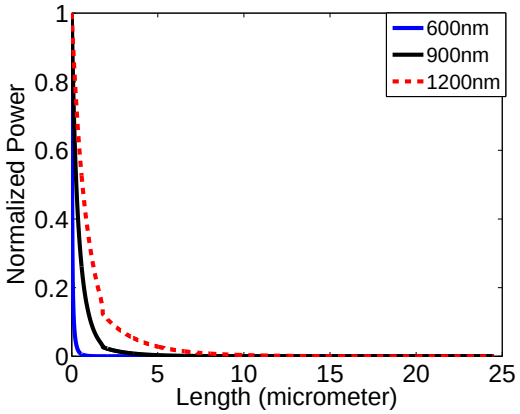

FIGURE 6.11: Normalized power curve for aluminum gallium arsenide.

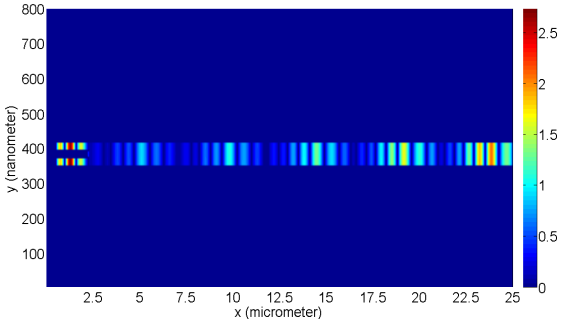

FIGURE 6.12: Electric field distribution inside the MDM waveguide with combiner.

6.3.2 Dielectric-Metal-Dielectric Waveguides

6.3.2.1 Formulations for the analysis

We investigate the symmetric SPP propagation properties in dielectric-metal-dielectric waveguide for different dielectric materials using the FDTD method. The properties we have focused on are SPP wavelength for different wavelengths of the input signal, field penetration depth into metal and dielectric layers and electric field strength at different distances from the interface of dielectric-metal. We have also analyzed these properties analytically and the obtained results are in good agreement with the numerical results. This study will be helpful in understanding the effect of symmetric SPP mode propagation in dielectric-metal-dielectric waveguides.

The SPP wavelength is given by,

$$\lambda_{SPP} = \lambda_o \sqrt{\frac{\varepsilon_d + \varepsilon'_m}{\varepsilon_d \varepsilon'_m}} \tag{6.7}$$

where, λ_o is the free space wavelength, ε_d is the real part of the complex relative permittivity of dielectric and ε'_m is the real part of the complex relative permittivity of metal. We have calculated the SPP wavelength using both equation and simulation. The obtained results were then compared and a very good agreement has been found between analytical and numerical results for all the materials that we have used.

The penetration depth into dielectric and metal are given by the following equations,

$$\delta_d = 1/k_o \left| (\varepsilon_d + \varepsilon'_m)/{\varepsilon_d}^2 \right|^{0.5} \tag{6.8}$$

$$\delta_m = 1/k_o \left| (\varepsilon_d + \varepsilon'_m)/{\varepsilon_m}^2 \right|^{0.5} \tag{6.9}$$

where, $k_o = 2\pi/\lambda_o$ is the wave vector for light in the free space.

The field penetration depths into metal and dielectric layers have been determined using the equations first for different input signal wavelengths. Then the same have been determined from the simulation and an excellent agreement has been found between the results obtained using the two techniques.

6.3.2.2 Simulation Results for DMD Waveguide

The schematic view of the metal-dielectric-metal waveguide that we have used for simulation is given in figure 6.13. The width of the metal layer has been taken as 60 nm and the width of both the dielectric layers as 500 nm. The profile pumped into the DMD waveguide is given in figure 6.14.

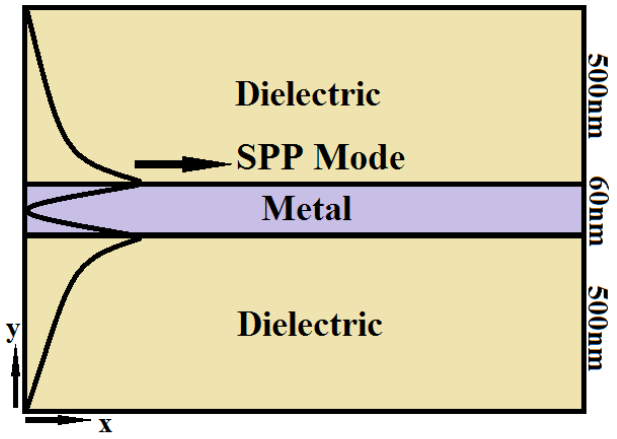

FIGURE 6.13: Schematic diagram of the DMD waveguide used for simulation.

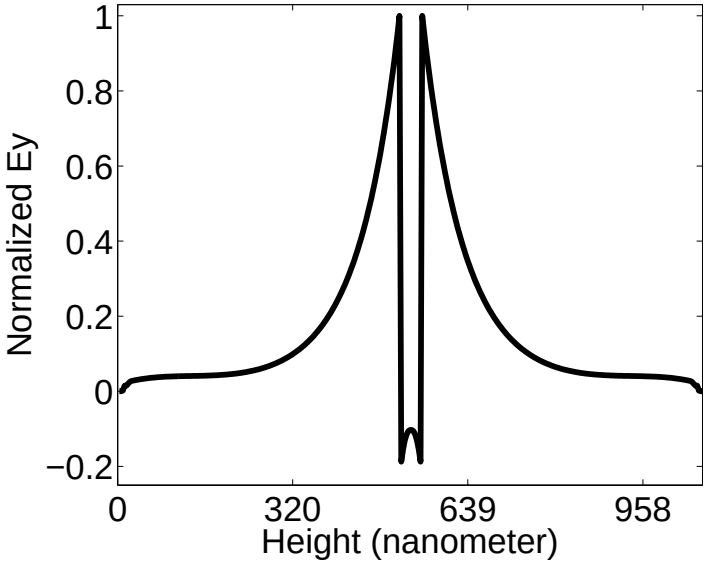

FIGURE 6.14: Ey profile pumped into the DMD waveguide.

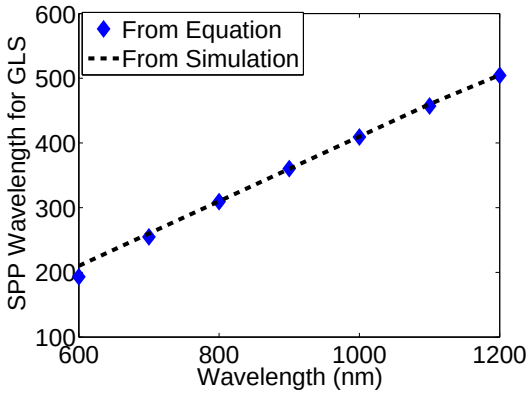

FIGURE 6.15: SPP wavelength calculated numerically and analytically for GLS.

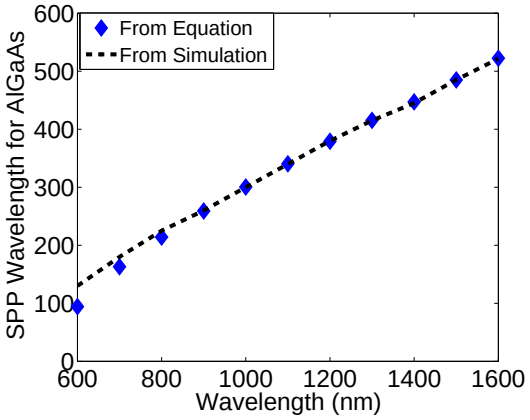

FIGURE 6.16: SPP wavelength calculated numerically and analytically for AlGaAs.

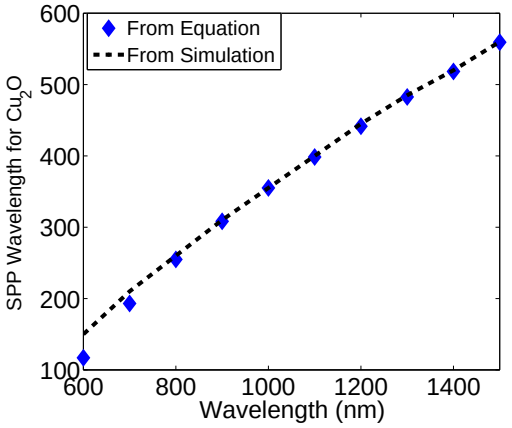

FIGURE 6.17: SPP wavelength calculated numerically and analytically for Cuprous Oxide.

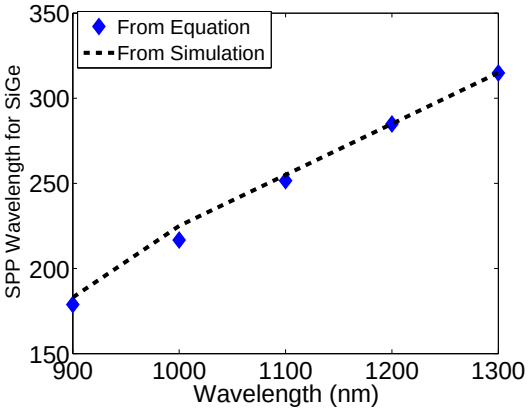

FIGURE 6.18: SPP wavelength calculated numerically and analytically for Si-Ge.

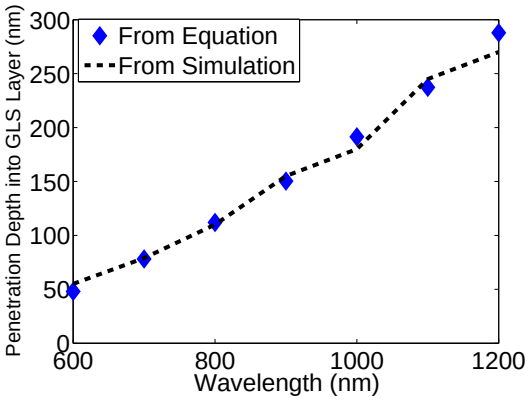

FIGURE 6.19: Penetration depth into GLS layer.

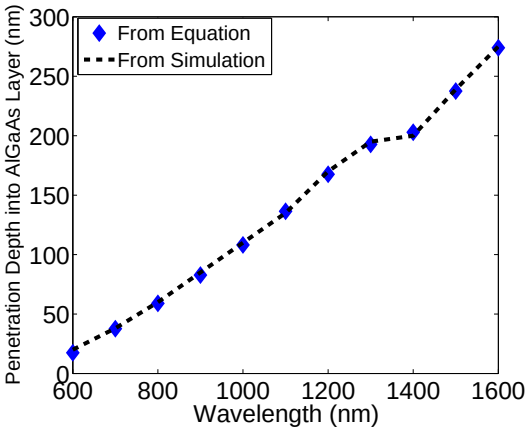

FIGURE 6.20: Penetration depth into AlGaAs layer.

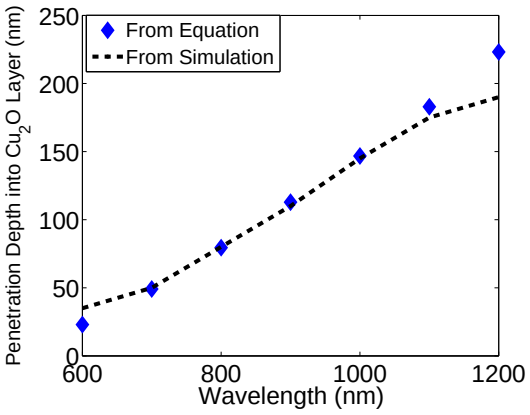

FIGURE 6.21: Penetration depth into Cuprous Oxide layer.

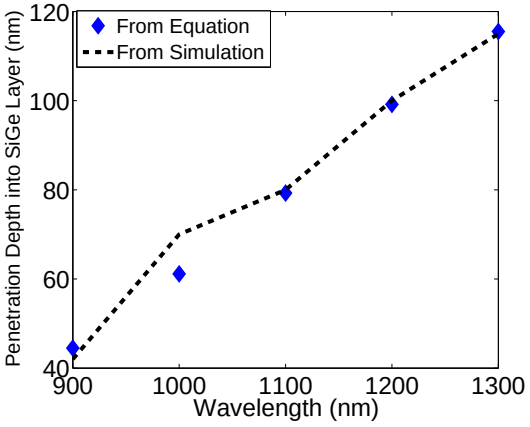

FIGURE 6.22: Penetration depth into Si-Ge layer.

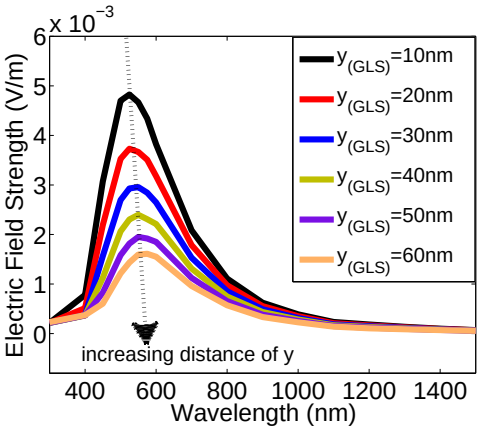

FIGURE 6.23: Electric field strength into GLS layer at different distances from the interface.

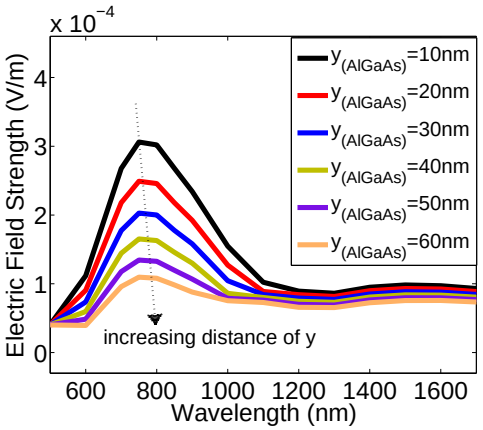

FIGURE 6.24: Electric field strength into AlGaAs layer at different distances from the interface.

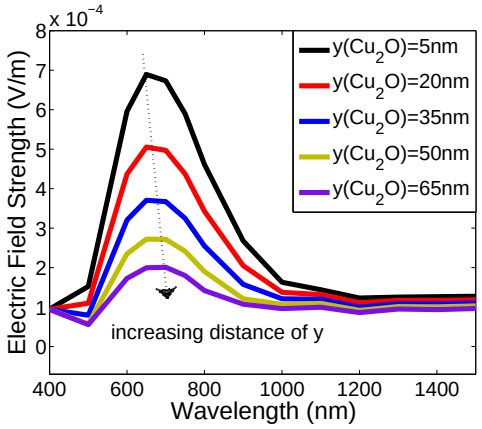

FIGURE 6.25: Electric field strength into Cuprous Oxide layer at different distances from the interface.

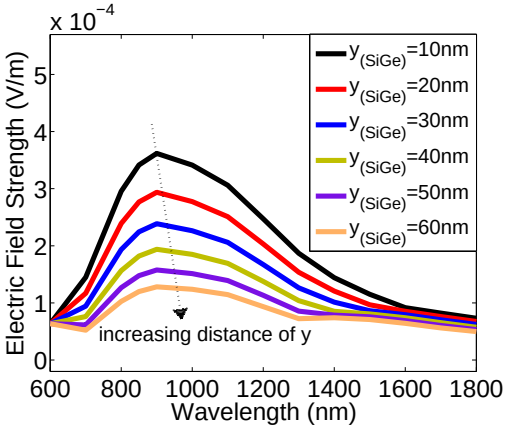

FIGURE 6.26: Electric field strength into SiGe layer at different distances from the interface.

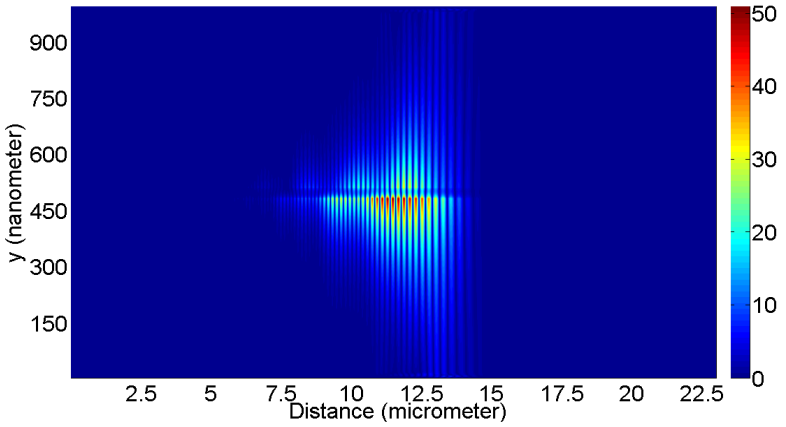

FIGURE 6.27: Electric field distribution inside the DMD waveguide used for simulation.

The minor disparity between the numerical and analytical results can be attributed to the difficulty in determining the exact location where the SPP gets matured. Also, in the simulation model, the material defining parameters are not 100% accurate.

In the SPP wavelength figures for different materials, it can be observed that the SPP wavelength is always less than the wavelength of the input signal that has excited the SPP. This observation is consistent with the theory. This is the reason SPP can overcome the diffraction limit.

The variations of electric field strength in at different distances from the dielectric-metal interface are presented in the figures. It can be observed that the electric field strength decreases as one goes away from the interface. This is the reason SPP mode field decreases exponentially in strength as one goes further from the interface in the y-direction. This happens due to the skin effect of the SPP mode in the metal and dielectric layers. The resonance mode is also clearly visible in the figures with peak amplitudes centered on different input signal wavelength for different materials.

6.3.3 Metal-Dielectric-Metal Waveguides

The metal-dielectric-metal configuration of the SPP waveguide is the most popular one since it can tightly squeeze the field in the dielectric region providing better confinement than other configurations. However, the power loss becomes higher due to increased overlapping with the metallic layer. Therefore, we have to optimize between confinement and power loss.

We have used different dielectric materials to construct the MDM waveguide and determined the power propagation distance. The schematic of the waveguide used for simulation is given in figure 6.28 and the Ey profile pumped into the waveguide is given in figure 6.29. The obtained normalized power curves for 1000 nm and 1200 nm wavelengths have been provided in figures 6.30 and 6.31. From the figures it can be observed that the propagation distance for GLS is the highest and for SiGe is the lowest. This observation can be explained using the imaginary part of the complex relative permittivity of these materials. The imaginary part of the complex relative permittivity of a material indicates the amount of loss of energy will occur in polarizing that particular material. Since the imaginary part of the complex relative permittivity of GLS is the smallest, the losses occur is the lowest among the materials we have used. On the other hand, the imaginary part of the complex relative permittivity of SiGe is the highest resulting in higher losses for polarization. Thus, GLS offers the highest propagation distance and SiGe offers the lowest propagation distance among all the dielectric materials that we have used.

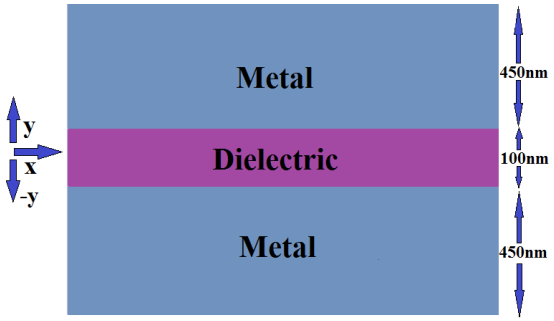

FIGURE 6.28: Schematic of the MDM waveguide used for simulation.

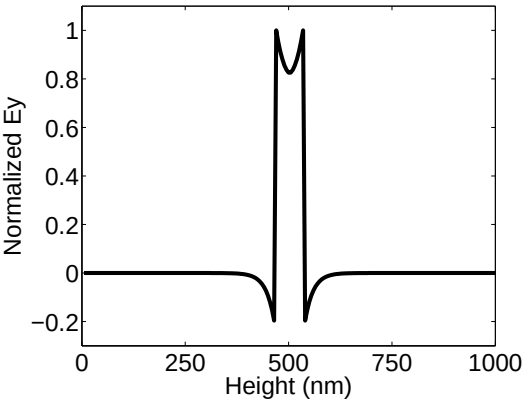

FIGURE 6.29: Ey profile pumped into the MDM waveguide.

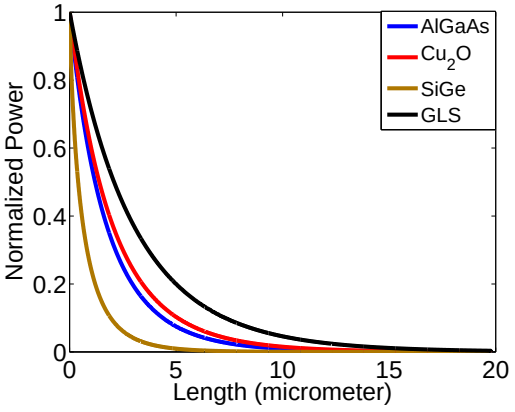

FIGURE 6.30: Normalized power curves for different materials for the input signal wavelength of 1000nm.

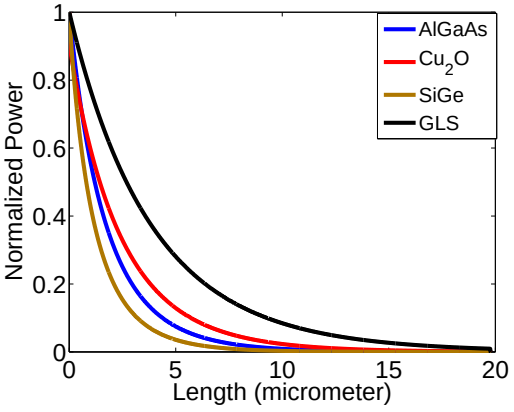

FIGURE 6.31: Normalized power curves for different materials for the input signal wavelength of 1200nm.

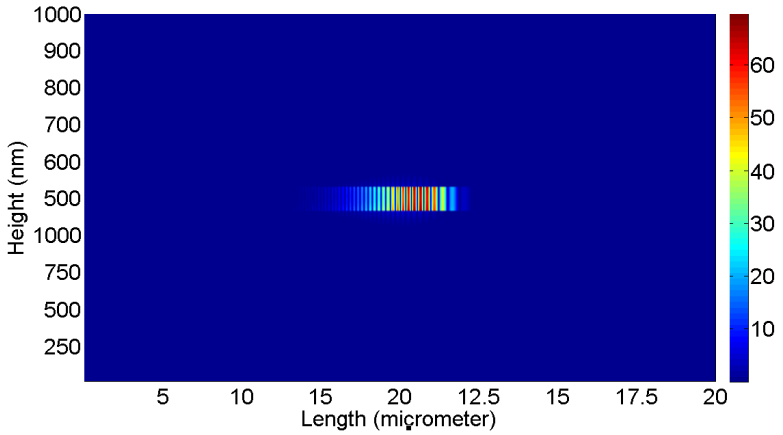

FIGURE 6.32: Electric field distribution inside the MDM waveguide.

6.3.4 Performance Analysis of Different Dielectrics as Nanoplasmonic Couplers

Nanoplasmonic couplers using gallium lanthanum sulfide (GLS) and cuprous oxide (Cu_2O) have been proposed and their characteristics and performance have been analyzed numerically using the finite-difference time-domain (FDTD) method. A coupling efficiency of 67% has been achieved at the optical communication wavelength when GLS is used as the coupler and a coupling efficiency of 56% has been achieved when cuprous oxide is used. The proposed nanoplasmonic couplers can operate at a broad frequency range. The design is also easier to fabricate since it is a flat terminal dielectric waveguide, placed at the entry of a plasmonic waveguide which is based on the metal-dielectric-metal (MDM) configuration.

6.3.4.1 Methodology of Analysis

The nanoplasmonic structure used for simulation is given in figure 6.33. Here the width of the GLS/Cu_2O layer is 500 nm and the width of the air layer in the MDM waveguide is 60 nm. The Ey profile pumped into the coupling structure is given in figure 6.34.

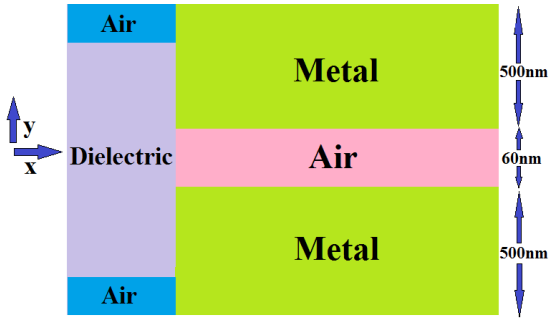

FIGURE 6.33: Schematic diagram of the coupling structure used for simulation.

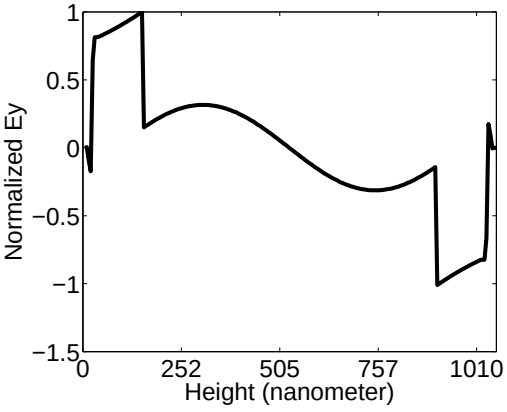

FIGURE 6.34: Ey profile pumped into the coupling structure.

6.3.4.2 Simulation Results and Discussion

We have defined the coupling efficiency as the ratio of the transmitted power into the MDM waveguide to the incident power in the input dielectric waveguide. The incident power of the fundamental mode has been measured right before the interface between dielectric and MDM waveguide and the transmitted power has been measured right after the interface.

We have also determined the reflection coefficient and return loss for both GLS and Cu_2O. The method we have used for calculating reflection coefficient is as follows. First an optical mode has been incident in the dielectric waveguide when there is no plasmonic waveguide. The value of the electric field is then recorded at one point. This represents the value of the incident wave. Then the same thing has been done with the plasmonic waveguide. This time the electric field represents the value of the incident wave plus the reflected wave. Therefore, we can calculate the reflected wave by subtracting the incident wave from this value. The reflection coefficient is then calculated by taking the maximum of the ratio of the reflected wave to the incident wave. This has been done for all the input signal wavelengths that we have simulated. The return loss for different wavelengths have been calculated using analytical equations from the numerically obtained reflection coefficient.

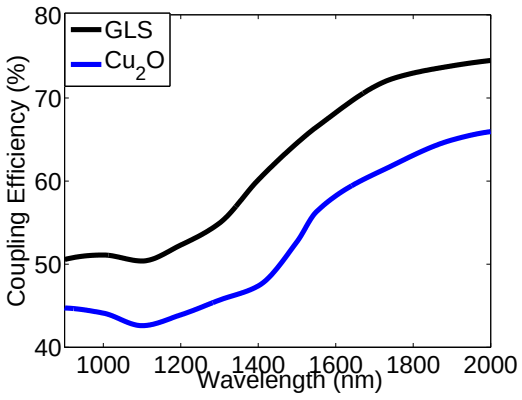

FIGURE 6.35: Efficiency as a function of wavelength for the proposed coupler.

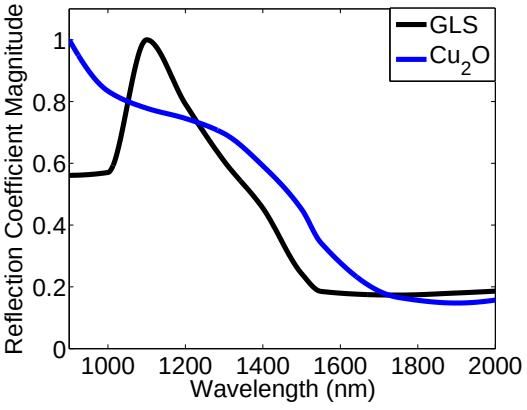

FIGURE 6.36: Reflection coefficient as a function of wavelength for the proposed coupler.

The coupling efficiency of the nanoplasmonic couplers using gallium lanthanum sulfide and cuprous oxide has been determined for different input signal wavelengths and presented in the figure 6.35. From the figure it can be observed that in all cases GLS provides better performance than Cu_2O and the efficiency keeps

on increasing as we increase the input signal wavelength reaching around 75% for GLS and around 66% for Cu_2O at the input signal wavelength of 2000 nm. The telecom wavelength which is 1550 nm, is of our particular interest since the laser sources that are used in optical communication technology is of this wavelength. At 1550 nm the efficiency of the coupler using GLS is 67% and for Cu_2O it is 56%.

The numerically calculated reflection coefficient has been given in figure 6.36. From the figure it can be observed that the reflection coefficient is the highest at the input signal wavelength of 1100 nm for GLS and for Cu_2O it keeps on decreasing as the input signal wavelength is increased. At telecom wavelength the magnitude of the reflection coefficient for GLS is 0.19 and for Cu_2O is 0.34. This indicates that at telecom wavelength most of the energy is coupled to the MDM waveguide from the dielectric waveguide.

The return loss is also determined using analytical equations from the numerically obtained reflection coefficient. From the figure 6.37 it can be observed that the return loss for GLS at 1550 nm wavelength is 14.64 dB whereas for Cu_2O it is 9.32 dB which are pretty good.

The electric field distributions inside the coupling structure for both gallium lanthanum sulfide and cuprous oxide have been presented in figures 6.38 and 6.39.

For comparison purpose, we have also provided the figures of the coupling structures proposed by Wahsheh [2] and Veronis [1]. From the figures it can be clearly understood that our proposed structure is very simple in comparison to the structures proposed by them.

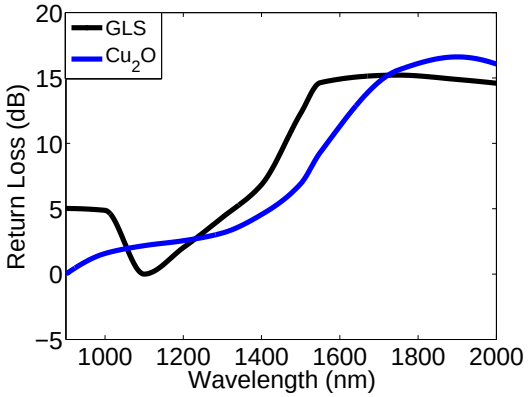

FIGURE 6.37: Return loss as a function of wavelength for the proposed coupler.

The coupler proposed by R. Wahsheh et al. [2] provides a theoretical efficiency of 50% at the telecommunication wavelength whereas our proposed coupler provides

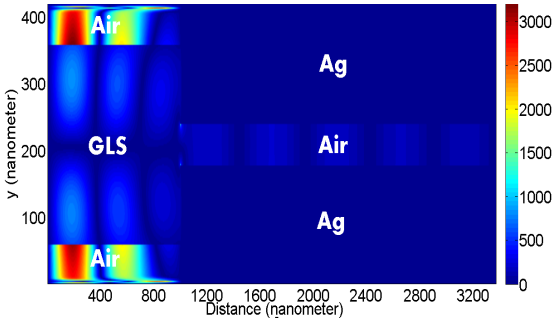

FIGURE 6.38: Electric field distribution inside the proposed coupler using GLS.

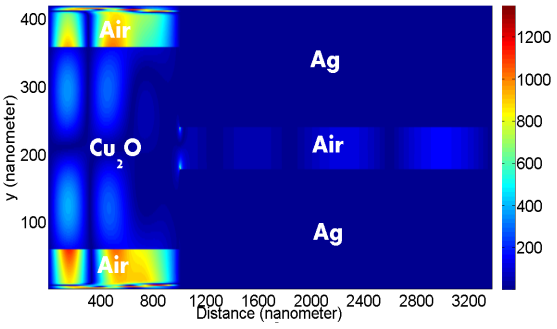

FIGURE 6.39: Electric field distribution inside the proposed coupler using Cu_2O.

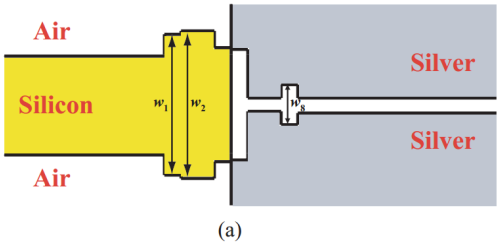

FIGURE 6.40: Coupler proposed by G. Veronis et al.[1].

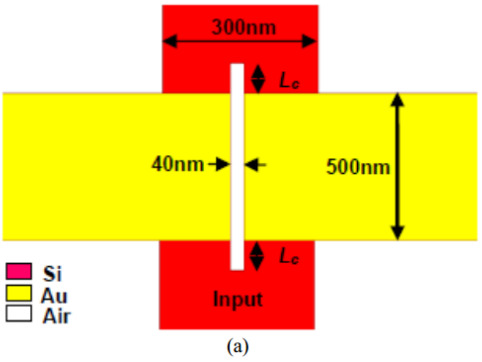

FIGURE 6.41: Coupler proposed by Rami A. Wahsheh et al. [2].

a theoretical efficiency of 67% for GLS and 56% for Cu_2O at the same input signal wavelength. The proposed couplers of G. Veronis [1] and D. Pile [32] contains tapering which is difficult to fabricate at the nano-scale. But our proposed structure is easier to fabricate since we have not used any tapered interface. Therefore, it is evident that our results are better than theirs.

Chapter 7

Conclusion and Future Works

7.1 Summary and Conclusion

In this thesis, the modeling parameters of different linear dispersive materials have been extracted and SPP propagation through different nanostructures has been investigated. The main contribution of this thesis is the extraction of modeling parameters for several materials and the analysis of a coupling structure using different materials. The thesis can be summarized as follows:

- An optimization method has been described using least-squares technique and the modeling parameters for several metals and dielectric materials have been extracted in the visible and near-IR range of the electromagnetic spectrum. The validation of the parameters has been done by comparing them with experimental values.
- A two dimensional simulation model based on the ADE-FDTD algorithm has been developed in order to simulate different optical nanostructures. The correctness of the simulation model has been checked by simulating with the parameters given by Taflove and comparing the results with the results provided by Taflove.
- A metal-dielectric-metal waveguide with a combiner constructed with different dielectric materials has been investigated. The combiner has been analyzed using different figure of merits such as reflection coefficient, return loss and voltage standing wave ratio.
- SPP propagation characteristics in different dielectric-metal-dielectric waveguide have been analyzed for different dielectric materials. The characteristics

that have been focused are SPP wavelength, SPP penetration depth and electric field strength at different distances from the metal-dielectric surface.

- Simple plasmonic coupling structures with GLS and Cu_2O have been proposed and analyzed. The couplers have been characterized by standard performance parameters like reflection coefficient and return loss. The couplers provide improved performance even though the structure is very simple.

7.2 Future Works

With the current progress of our work, we have several future goals that we want to achieve.

- The numerical simulator developed in this work is powerful in the sense that it is capable of simulating unlimited number of devices and structures containing linear dispersion.
- We will work with nonlinear materials and try to extract their modeling parameters in order to include them in our simulator.
- The current numerical simulator can be extended to 3D to observe the linear dispersion of different nanostructures.
- We will try to arrange some experimental setups and implement our work practically.

Bibliography

[1] G. Veronis and S. Fan, "Theoretical investigation of compact couplers between dielectric slab waveguides and two-dimensional metal-dielectric-metal plasmonic waveguides," *Opt. Express*, vol. 15, no. 3, pp. 1211–1221, 2007.

[2] R. Wahsheh, Z. Lu, and M. Abushagur, "Nanoplasmonic air-slot coupler: Design and fabrication," in *Frontiers in Optics*. Optical Society of America, 2012.

[3] S. A. Maier, "Plasmonics: metal nanostructures for subwavelength photonic devices," *Selected Topics in Quantum Electronics, IEEE Journal of*, vol. 12, no. 6, pp. 1214–1220, 2006.

[4] ——, "Plasmonics: The promise of highly integrated optical devices," *Selected Topics in Quantum Electronics, IEEE Journal of*, vol. 12, no. 6, pp. 1671–1677, 2006.

[5] D. K. Gramotnev and S. I. Bozhevolnyi, "Plasmonics beyond the diffraction limit," *Nature Photonics*, vol. 4, no. 2, pp. 83–91, 2010.

[6] W. L. Barnes, A. Dereux, and T. W. Ebbesen, "Surface plasmon subwavelength optics," *Nature*, vol. 424, no. 6950, pp. 824–830, 2003.

[7] A. Kriesch, S. P. Burgos, D. Ploss, H. Pfeifer, H. A. Atwater, and U. Peschel, "Functional plasmonic nano-circuits with low insertion and propagation losses," *Nano letters*, 2013.

[8] S. Y. Chou and W. Ding, "Ultrathin, high-efficiency, broad-band, omni-acceptance, organic solar cells enhanced by plasmonic cavity with subwavelength hole array," *Optics Express*, vol. 21, no. 101, pp. A60–A76, 2013.

[9] S.-S. Kim, S.-I. Na, J. Jo, D.-Y. Kim, and Y.-C. Nah, "Plasmon enhanced performance of organic solar cells using electrodeposited ag nanoparticles," *Applied Physics Letters*, vol. 93, p. 073307, 2008.

[10] S. Pillai, K. Catchpole, T. Trupke, and M. Green, "Surface plasmon enhanced silicon solar cells," *Journal of applied physics*, vol. 101, p. 093105, 2007.

[11] R. J. Blaikie and D. O. Melville, "Imaging through planar silver lenses in the optical near field," *Journal of Optics A: Pure and Applied Optics*, vol. 7, no. 2, p. S176, 2005.

[12] D. O. Melville, R. J. Blaikie, and C. Wolf, "Super-resolution imaging through a planar silver layer," *Opt. Express*, vol. 13, no. 6, pp. 2127–2134, 2005.

[13] S. Kawata, Y. Inouye, and P. Verma, "Plasmonics for near-field nano-imaging and superlensing," *nature photonics*, vol. 3, no. 7, pp. 388–394, 2009.

[14] X. Zhang and Z. Liu, "Superlenses to overcome the diffraction limit," *Nature materials*, vol. 7, no. 6, pp. 435–441, 2008.

[15] A. J. Haes and R. P. Van Duyne, "A unified view of propagating and localized surface plasmon resonance biosensors," *Analytical and Bioanalytical Chemistry*, vol. 379, no. 7-8, pp. 920–930, 2004.

[16] A. Hosseini and Y. Massoud, "A low-loss metal-insulator-metal plasmonic bragg reflector," *Optics express*, vol. 14, no. 23, pp. 11 318–11 323, 2006.

[17] J. Henzie, M. H. Lee, and T. W. Odom, "Multiscale patterning of plasmonic metamaterials," *Nature nanotechnology*, vol. 2, no. 9, pp. 549–554, 2007.

[18] S. A. Maier, *Plasmonics: fundamentals and applications*. Springer, 2007.

[19] E. Verhagen, "Subwavelength light confinement with surface plasmon polaritons," 2009.

[20] R. Petit, "Electromagnetic theory of gratings," *Electromagnetic Theory of Gratings. Series: Topics in Current Physics, ISBN: 978-3-642-81502-7. Springer Berlin Heidelberg (Berlin, Heidelberg), Edited by Roger Petit, vol. 22*, vol. 22, 1980.

[21] H. Raether, *Surface plasmons on smooth surfaces*. Springer, 1988.

[22] A. Archambault, T. V. Teperik, F. Marquier, and J.-J. Greffet, "Surface plasmon fourier optics," *Physical Review B*, vol. 79, no. 19, p. 195414, 2009.

[23] E. Jin and X. Xu, "Plasmonic effects in near-field optical transmission enhancement through a single bowtie-shaped aperture," *Applied Physics B*, vol. 84, no. 1-2, pp. 3–9, 2006.

[24] J. T. Krug II, E. J. Sánchez, and X. S. Xie, "Design of near-field optical probes with optimal field enhancement by finite difference time domain electromagnetic simulation," *The Journal of chemical physics*, vol. 116, p. 10895, 2002.

[25] W. H. Pernice, F. P. Payne, and D. F. Gallagher, "A general framework for the finite-difference time-domain simulation of real metals," *Antennas and Propagation, IEEE Transactions on*, vol. 55, no. 3, pp. 916–923, 2007.

[26] A. D. Rakic, A. B. Djurišic, J. M. Elazar, and M. L. Majewski, "Optical properties of metallic films for vertical-cavity optoelectronic devices," *Applied optics*, vol. 37, no. 22, pp. 5271–5283, 1998.

[27] M. A. Ordal, R. J. Bell, R. Alexander Jr, L. Long, M. Querry *et al.*, "Optical properties of fourteen metals in the infrared and far infrared: Al, co, cu, au, fe, pb, mo, ni, pd, pt, ag, ti, v, and w." *Applied Optics*, vol. 24, no. 24, pp. 4493–4499, 1985.

[28] G. Veronis and S. Fan, "Bends and splitters in metal-dielectric-metal subwavelength plasmonic waveguides," *Applied Physics Letters*, vol. 87, no. 13, pp. 131 102–131 102, 2005.

[29] H. Gao, H. Shi, C. Wang, C. Du, X. Luo, Q. Deng, Y. Lv, X. Lin, and H. Yao, "Surface plasmon polariton propagation and combination in y-shaped metallic channels," *Optics Express*, vol. 13, no. 26, pp. 10 795–10 800, 2005.

[30] B. Wang and G. P. Wang, "Surface plasmon polariton propagation in nanoscale metal gap waveguides," *Optics letters*, vol. 29, no. 17, pp. 1992–1994, 2004.

[31] P. Ginzburg and M. Orenstein, "Plasmonic transmission lines: from micro to nano scale with $\lambda/4$ impedance matching," *Optics Express*, vol. 15, no. 11, pp. 6762–6767, 2007.

[32] D. Pile and D. K. Gramotnev, "Adiabatic and nonadiabatic nanofocusing of plasmons by tapered gap plasmon waveguides," *Applied Physics Letters*, vol. 89, no. 4, p. 041111, 2006.

[33] R. Luebbers, F. P. Hunsberger, K. S. Kunz, R. B. Standler, and M. Schneider, "A frequency-dependent finite-difference time-domain formulation for dispersive materials," *Electromagnetic Compatibility, IEEE Transactions on*, vol. 32, no. 3, pp. 222–227, 1990.

[34] D. F. Kelley and R. J. Luebbers, "Piecewise linear recursive convolution for dispersive media using fdtd," *Antennas and Propagation, IEEE Transactions on*, vol. 44, no. 6, pp. 792–797, 1996.

[35] R. J. Luebbers, F. Hunsberger, and K. S. Kunz, "A frequency-dependent finite-difference time-domain formulation for transient propagation in plasma," *Antennas and Propagation, IEEE Transactions on*, vol. 39, no. 1, pp. 29–34, 1991.

[36] R. J. Luebbers and F. Hunsberger, "Fdtd for¡ e1¿ n¡/e1¿ th-order dispersive media," *Antennas and Propagation, IEEE Transactions on*, vol. 40, no. 11, pp. 1297–1301, 1992.

[37] F. Hunsberger, R. Luebbers, and K. Kunz, "Finite-difference time-domain analysis of gyrotropic media. i. magnetized plasma," *Antennas and Propagation, IEEE Transactions on*, vol. 40, no. 12, pp. 1489–1495, 1992.

[38] C. Melon, P. Leveque, T. Monediere, A. Reineix, and F. Jecko, "Frequency dependent finite-difference–time-domain [(fd) 2td] formulation applied to ferrite material," *Microwave and Optical Technology Letters*, vol. 7, no. 12, pp. 577–579, 1994.

[39] A. Akyurtlu and D. H. Werner, "Bi-fdtd: A novel finite-difference time-domain formulation for modeling wave propagation in bi-isotropic media," *Antennas and Propagation, IEEE Transactions on*, vol. 52, no. 2, pp. 416–425, 2004.

[40] A. Grande, I. Barba, A. C. Cabeceira, J. Represa, P. P. So, and W. J. Hoefer, "Fdtd modeling of transient microwave signals in dispersive and lossy bi-isotropic media," *Microwave Theory and Techniques, IEEE Transactions on*, vol. 52, no. 3, pp. 773–784, 2004.

[41] A. Akyurtlu and D. H. Werner, "A novel dispersive fdtd formulation for modeling transient propagation in chiral metamaterials," *Antennas and Propagation, IEEE Transactions on*, vol. 52, no. 9, pp. 2267–2276, 2004.

[42] E. D. Palik, *Handbook of Optical Constants of Solids: Index*. Access Online via Elsevier, 1998, vol. 3.

[43] K. Yee, "Numerical solution of initial boundary value problems involving maxwell's equations in isotropic media," *Antennas and Propagation, IEEE Transactions on*, vol. 14, no. 3, pp. 302–307, 1966.

[44] M. A. Alsunaidi and A. A. Al-Jabr, "A general ade-fdtd algorithm for the simulation of dispersive structures," *Photonics Technology Letters, IEEE*, vol. 21, no. 12, pp. 817–819, 2009.

[45] J.-P. Berenger, "A perfectly matched layer for the absorption of electromagnetic waves," *Journal of computational physics*, vol. 114, no. 2, pp. 185–200, 1994.

[46] A. Taflove and S. C. Hagness, "Computationai electrodynamics," 1995.

[47] M. Alsunaidi and F. Al-Hajiri, "Time-domain analysis of wideband optical pulse shg in layered dispersive material," *Proceedings of the Progress in Electromagnetic Research, Beijing, China*, pp. 1694–1697, 2009.

[48] R. HasanSagor, "Plasmon enhanced symmetric mode generation in metal-insulator-metal structure with kerr nonlinear effect," *International Journal of Computer Applications*, vol. 50, no. 18, pp. 24–28, 2012.